Reviewed research article

The destabilization of a large mountain slope controlled by thinning of Svínafellsjökull glacier, SE Iceland

Daniel Ben-Yehoshua[1], Þorsteinn Sæmundsson[2,3], Sigurður Erlingsson[1], Jón Kristinn Helgason[4], Reginald L. Hermanns[5,6], Eyjólfur Magnússon[3], Benedikt G. Ófeigsson[4], Joaquín M.C. Belart[7], Ásta Rut Hjartardóttir[3], Halldór Geirsson[3], Snævarr Guðmundsson[8], Hrafnhildur Hannesdóttir[4], Finnur Pálsson[3], Vincent Drouin[4], and Bergur H. Bergsson[4]

[1]*Faculty of Civil and Environmental Engineering, University of Iceland, Reykjavík, Iceland*

[2]*Faculty of Life and Environmental Sciences, Department of Geography and Tourism, University of Iceland*

[3]*Institute of Earth Sciences, University of Iceland, Reykjavík, Iceland*

[4]*Icelandic Meteorological Office, Reykjavík, Iceland*

[5]*Geological Survey of Norway, Leiv Eiriksonsvei 39, 7040 Trondheim, Norway*

[6]*Department of Geoscience and Petroleum, Norwegian University of Science and Technology, S. P. Andersensveg 15a, 7031 Trondheim, Norway*

[7]*National Land Survey of Iceland, Akranes, Iceland*

[8]*South East Iceland Nature Research Center, Höfn in Hornafjörður, Iceland*

Corresponding author dby@hi.is; https://doi.org/10.33799/jokull2023.73.001

Abstract — *Since the end of the 19th century Iceland's glaciers have experienced significant ice-mass loss. Thinning glaciers expose oversteepened rock walls which may adjust in the form of paraglacial rock slope failures. Here we highlight a cluster of gravitational mass movements around the margin of the Svínafellsjökull outlet glacier in Southeast Iceland. The largest slope instability is located in an area called Svarthamrar on the northern slope of Mt. Svínafellsfjall and is evidenced by a 2 km-long fracture system that affects an area of about 0.9 km^2 and a minimum rock volume in the range of 50–150$\times$10^6 m^3. The Svarthamrar slope instability is characterized by about 200 sinkholes where the soil cover collapsed into underlying bedrock fractures. Remote sensing data and field mapping indicate that the onset of this deformation occurred between 2003 and 2007, during the period of the most rapid glacier thinning within the 131-year record. Since 2011 the glacier surface has not thinned significantly, in part due to a large debris avalanche in 2013 forming a sheet of debris on the glacier. The debris protects the glacier against ablation and adds about 12$\times$10^6 t of load onto the subglacial slope. The slope showed signs of deformation until 2017. No significant movement has been detected since the installation of a monitoring network in 2018 and 2019 suggesting that the slope has temporarily regained equilibrium. However, with future glacial thinning the slope is likely to continue destabilizing. Large rockslide scars in the valley flanks above the glacier and bulky end moraine deposits composed of angular boulder material suggest previous rock slope failures in the catchment. Current rock surface temperatures on site, and back-calculated temperatures suggest that it is unlikely that permafrost occurs on the site or has played a role in the evolution of the Svarthamrar slope instability. This study expands the understanding of the driving forces of unstable paraglacial slopes and emphasizes that climate change driven glacier thinning has and likely will have further destabilizing effects on this slope and other paraglacial slopes in Iceland and elsewhere.*

INTRODUCTION

Since the Little Ice Age (LIA), global warming has led to glacier retreat across the globe (Meredith *et al.*, 2019; Zemp *et al.*, 2019; Hugonnet *et al.*, 2021). As glaciers retreat out of alpine valleys, surrounding slopes will adjust to the new physical conditions (Grämiger *et al.*, 2017; Deline *et al.*, 2021) which can result in stark morphological changes. Paraglacial landslides during and shortly after deglaciation have been described in numerous publications (Ballantyne, 2002; McColl, 2012; Hermanns *et al.*, 2017; Porter *et al.*, 2019; Lacroix *et al.*, 2022). Slope failure in these environments occurs usually due to a combination of static boundary conditions (non-changing) such as structural weaknesses and dynamic boundary conditions (changing over longer timeframes) along with short term triggering factors such as an increase in pore-water pressure or seismic events (Hermanns *et al.*, 2006). However, triggering events are not always necessary as slopes can also fail as the result of progressive rock failure (Eberhardt *et al.*, 2004; Hermanns and Longva, 2013; Stead and Eberhardt, 2013).

Climate warming affects the dynamic boundary conditions through temperature increase and changed precipitation patterns, which can lead to destabilizing boundary conditions such as glacial debuttressing, unloading, exposure of the slope to atmospheric weathering, permafrost thaw, and hydrological changes (Evans and Clague, 1994). Glacial debuttressing and unloading describe the reduction of mechanical slope support as glaciers thin along valley walls (McColl and Davies, 2013; Deline *et al.*, 2021). Debuttressing and unloading can additionally lead to significant pressure release in the bedrock which can cause fractures and maturation of faults (Grämiger *et al.*, 2017; Hartmeyer *et al.*, 2020).

Thermomechanical damage and thus weakening of rock slopes occurs through cycles of changing glacier cover (Grämiger *et al.*, 2017) and exposure to different thermal regimes and atmospheric erosive factors (Grämiger *et al.*, 2018). Apart from glacial retreat, other cryospheric changes such as permafrost degradation (Bessette-Kirton and Coe, 2020; Hilger *et al.*, 2021; Etzelmüller *et al.*, 2022; Penna *et al.*, 2022) and hydrologic changes (Gruber and Haeberli, 2008; Hasler *et al.*, 2011; Chiarle *et al.*, 2021) have been shown to accelerate the destabilization of mountain slopes.

Due to the lower density of glacier ice and its viscoplastic nature, deformation or failure of the remaining glacier ice can occur when a failure surface extends below the glacier surface (Evans and Clague, 1988; McColl and Davies, 2013; Storni *et al.*, 2020). Large slope deformations, which are somewhat controlled by glacial retreat, have been observed in Switzerland (Kos *et al.*, 2016), Alaska (Dai *et al.*, 2020) and Iceland (Lacroix *et al.*, 2022). The timing of slope destabilization seems to be controlled by the time scale of the bedrock damage compared to the glacier thinning rate (Lacroix and Amitrano, 2013), the scale of the moving mass (McColl and Davies, 2013), the valley geometry (Spreafico *et al.*, 2021) and ice rheology (Storni *et al.*, 2020). Slope deformation is typically initiated with time lag to glacial thinning (Lacroix and Amitrano, 2013; Kos *et al.*, 2016; Grämiger *et al.*, 2017). This lag can be up to several tens of thousands of years, with the likelihood of failure declining with time since glaciation (Cruden and Hu, 1993; Evans and Clague, 1994; Soldati *et al.*, 2004). Systematic studies in Scotland and Norway, observe a peak of rock slope failures in the first millennia after rapid temperature increases in combination with deglaciation (Ballantyne *et al.*, 2014; Böhme *et al.*, 2015; Hermanns *et al.*, 2017). This suggests that the most likely period of a catastrophic failure is during and right after deglaciation. Paraglacial mass movements range from small scale rock falls and debris flows to mountain scale deep-seated gravitational slope deformations. Very large unstable slopes often deform with extremely slow movement rates (millimeters or less per year), but a part of the creeping mass can evolve into multiple partial failures or into fast large catastrophic slope failures (Agliardi *et al.*, 2012). Catastrophic large-scale landslides can have a powerful impact on the glaciers and the surrounding areas (Hewitt *et al.*, 2011; Reznichenko *et al.*, 2012; Soldati, 2013; Deline *et al.*, 2014; Hermanns *et al.*, 2015; Dufresne *et al.*, 2019). Large landslides onto glaciers may travel with high velocities and have exceptionally long runouts (Deline *et al.*, 2014). If their runout continues beyond the glacier margin, secondary hazards emerge that often pose a more significant threat to humans (Huggel *et al.*, 2005; Evans *et al.*, 2009; Shugar *et al.*, 2021). These threats include displacement waves due to a landslide entering a body of water (Stoffel and Huggel, 2012; Dufresne *et al.*, 2018; Svennevig *et al.*, 2020, 2023; Geertsema *et al.*, 2022) or flooding due to a valley-blocking landslide dam formation and failure of these dams (Fan *et al.*, 2020).

GEOGRAPHIC AND GEOLOGICAL SETTING

Iceland is a volcanic island in the North Atlantic Ocean with most of the country's bedrock consisting of layered effusive lavas. However, since glaciations started in the quaternary, water- and ice-contact volcanism produced large amounts of tuffaceous rocks, especially around the active volcanic centers (Helgason and Duncan, 2001; Thordarson and Larsen, 2007; Jakobsson and Guðmundsson, 2008).

During the Last Glacial Maximum (LGM) Iceland was covered by an up to 2000 m thick ice sheet which collapsed in the late Pleistocene and early Holocene and left smaller icecaps and valley glaciers behind (Norðdahl and Ingólfsson, 2015) covering about 10% of the country nowadays (Aðalgeirsdóttir *et al.*, 2020). Landslide deposits are ubiquitous to many of Iceland's mountain valleys (Jónsson, 1974) with many of them dating back to the time of deglaciation or shortly after (Cossart *et al.*, 2013; Mercier *et al.*, 2013; Coquin *et al.*, 2015; Decaulne *et al.*, 2016; Peras *et al.*, 2016).

Since the end of the LIA in Iceland at around 1890, Icelandic glaciers have lost about 16% (540 ± 130 Gt) of their mass, half of which disappeared between 1994 and 2019 (Aðalgeirsdóttir *et al.*, 2020). In front of many of the outlet glaciers deep pro-glacial lakes have been forming (Guðmundsson *et al.*, 2019). Temperature records show strong warming episode in the 1920's and 1930's and a subsequent period of slight cooling that lasted until the mid-1980's (Björnsson *et al.*, 2018). Consequently, most glaciers in Iceland were either close to equilibrium, or in slight surplus from $\sim$1960 to the early 1990's. From 1994 until 2010, warming lead to rapid glacier-ice loss of $\sim$12 Gt/yr (Aðalgeirsdóttir *et al.*, 2020; Belart *et al.*, 2020), but since then the loss rate has been reduced to $\sim$6 Gt/yr (Aðalgeirsdóttir *et al.*, 2020; Pálsson *et al.*, 2022).

In recent decades several paraglacial landslides in Icelandic glacial valleys have been documented. Some occurred catastrophically with only a few years or no documented precursory activity (Kjartansson, 1967; Sigurdsson and Williams, 1991; Decaulne *et al.*, 2010; Sæmundsson *et al.*, 2011; Ben-Yehoshua *et al.*, 2022) and other paraglacial slopes have deformed gradually somewhat controlled by glacier retreat but still within a decadal timeframe (Arnar, 2021; Lacroix *et al.*, 2022). Large paraglacial failures (>10^7 m^3) often form vertical head scarps of 200–300 m in height and a rotational failure plane (Kjartansson, 1967; Lacroix *et al.*, 2022).

In addition, outside of glaciated regions several large catastrophic landslides have been reported over the last decade which were related to permafrost thawing (Helgason *et al.*, 2018; Sæmundsson *et al.*, 2018; Morino *et al.*, 2019, 2021), prolonged periods of precipitation (Schöpa *et al.*, 2018; Dabiri *et al.*, 2020) and inherent structural features in combination with hydrothermal alteration (Schöpa *et al.*, 2018).

The research area (Figure 1) for the presented study lies on the western flank of the active stratovolcano Öræfajökull (2110 m a.s.l.). The volcano is covered by the Öræfajökull Ice Cap in the southernmost part of the Vatnajökull Ice Cap in SE Iceland. The Öræfajökull Ice Cap is drained by numerous outlet glaciers. One of these outlet glaciers on the volcano's western flanks is Svínafellsjökull. The study site is located on a mountain ridge that runs from southwest to northeast for about 5 km along the southern margin of Svínafellsjökull. This mountain ridge has three main summits called Svínafellsfjall (846 m a.s.l.), Öskuhnúta (917 m a.s.l.) and Skarðatindur (1084 m a.s.l.). Steep slopes and cliffs are found close to the ridge line and at the Svínafellsjökull glacier margin. However, most of the area between the ridge and Svínafellsjökull is characterized by a west and northwest facing,

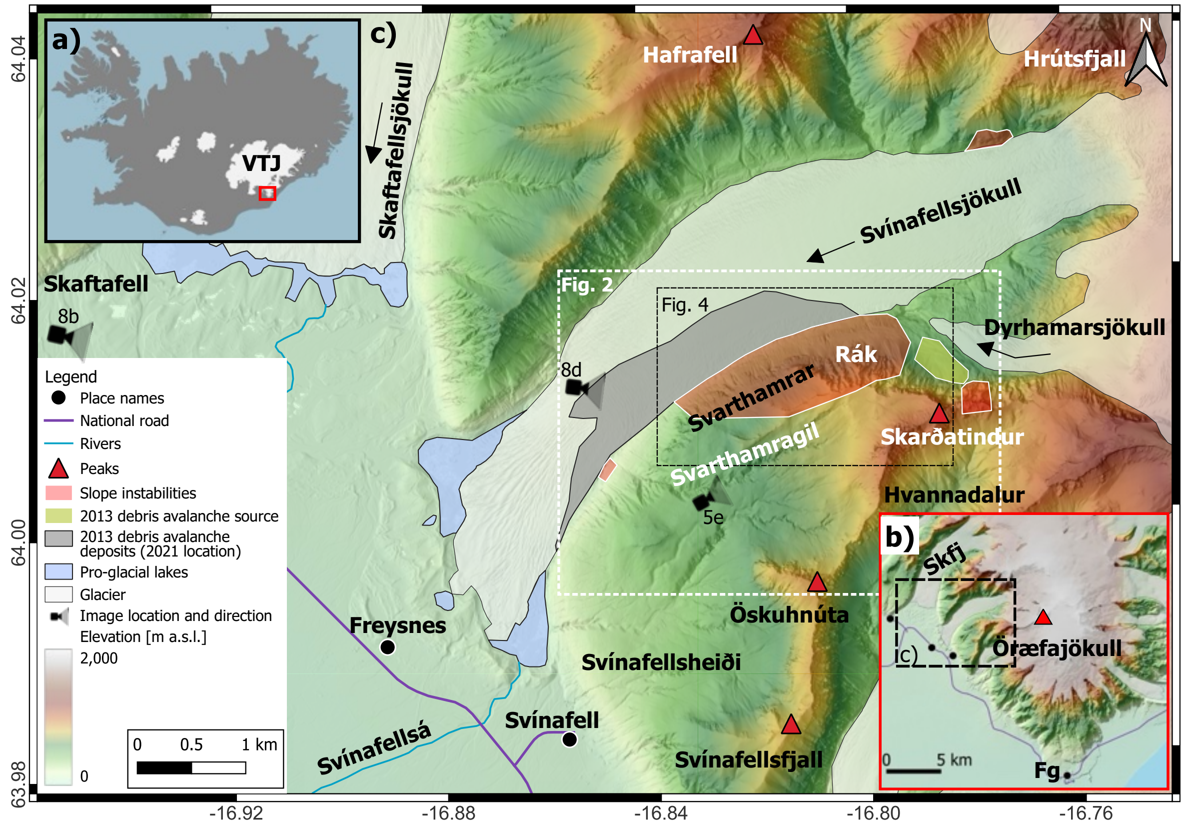

Figure 1. Location map of the study area in SE Iceland (a,b,c). Black arrows (c) indicate the glacier flow direction. The grey polygon on Svínafellsjökull shows the extent and location of the 2013 debris avalanche deposits in 2021. The pro-glacial lake extent is based on 2021 elevation data. The camera icons indicate approximate locations and directions of photographs with respective figure numbers. Abbreviations used: VTJ – Vatnajökull ice cap; Skfj – Skaftafellsjökull; Fg – Fagurhólsmýri. Road lines, and glacier extents (modified) are from the database of the National Land Survey of Iceland (LMÍ). The hillshade DEM is from Jóhannesson *et al.* (2013). Coordinates are in the WGS84 reference frame. – *Staðsetning rannsóknasvæðsins á suðausturlandi (a,b,c). Svartar örvar sýna flæðistefnu jöklanna. Gráskyggða svæðið á Svínafellsjökli afmarkar útbreiðslu efnisins úr skriðunni árið 2021, en skriðan féll árið 2013. Útmörk jökullónanna er byggð á hæðargögnum frá árinu 2021. Myndavélatákn sýna staðsetningu og stefnu ljósmynda á myndum 7b,d og 5e. Skammstafanir: VTJ – Vatnajökull; Skfj – Skaftafellsjökull; Fg – Fagurhólsmýri. Veglínur, hæðargögn og stærð jöklanna (breytt) eru úr gagnagrunni Landmælinga Íslands. Hæðarlíkan er frá Jóhannesson et al. (2013). Lengdar- og breiddargráður eru samkvæmt WGS84 kerfinu.*

gently inclined plateau between 300 and 900 m a.s.l., that is cut by several canyons. The most prominent of those canyons is called Svarthamragil which runs for about 2 km southwest and then turns to the northwest and drains into the lateral margin of Svínafellsjökull. Enclosed by Svarthamragil canyon in the south and Svínafellsjökull in the north lies a slope called Svarthamrar where the main signs for slope instability are located which are discussed in this article. We will refer to the unstable slope as Svarthamrar slope instability and to the whole mountain as Svínafellsfjall.

The bedrock on Svínafellsfjall consists of rock sequences dominated by subglacial volcanism and intermitted by subaerial volcanism and glacial sediments younger than 0.8 Ma, resting on eroded lavas of Neogene age (Helgason and Duncan, 2001, 2013). Glacial activity in the valley repeatedly eroded the mountainside and younger volcanics and sediments were deposited on these erosive surfaces. The youngest rocks in the area of the Svarthamrar slope instability were deposited on a northwest sloping erosive contact (Helgason and Duncan, 2013).

Volcanic activity of Öræfajökull during the Holocene is fairly well constrained (Guðmundsson, 1998) and since the settlement of Iceland (874 AD) two eruptions (1362 and 1727) are documented (Thorarinsson, 1958; Roberts and Gudmundsson, 2015). Precursory earthquakes, as well as jökulhlaups, lahars and tephra fallouts occurred during both eruptions (Thorarinsson, 1958; Gudmundsson *et al.*, 2008; Sharma *et al.*, 2008; Einarsson, 2019). At the end of 2016 seismic activity increased at the volcano, culminating by the end of 2018, which has been explained by magma intrusions into the volcanic system. Since 2018 seismic activity at the volcano has been decreasing (Geirsson *et al.*, 2018; Jónsdóttir *et al.*, 2018). As a response to the glacier loss over the last decades glacio-isostatic adjustment has caused a vertical uplift of around 30 mm/yr around Öræfajökull (Drouin and Sigmundsson, 2019).

Svínafellsjökull and its foreland

Svínafellsjökull is a 7.5 km long outlet glacier emerging from an ice fall which drains on the western side of the Öræfajökull Ice Cap (Figure 1). The uppermost part of the glacier is a wide ice fall where the strongly crevassed glacier flows down approximately 1000 vertical meters over a distance of about 1500 m. According to Hannesdóttir *et al.* (2015) the glacier lost about 30% of its volume between 1890 and 2010 and its surface area decreased by about 16%. From 1890 to 2011 the ice thickness in the central part of the glacier has lowered by about 100 m. The central part of the snout retreated about 750 m between 1890 and 1945 (Guðmundsson *et al.*, 2019). Between 1945 and 2011, the central glacier margin has thinned by about 75 m, but the retreat of the central glacier front was only about 100 m during that time interval (Hannesdóttir *et al.*, 2015; Guðmundsson *et al.*, 2019). Even though the central part of the frontal glacier margin has been somewhat stagnant since around 2011 the northern and southern end of the margin continue to retreat which led to the formation of two pro-glacial lakes (Figure 1) around the year 2000 and reaching an estimated combined volume of ca. 10^7 m^3 by 2018 (Guðmundsson *et al.*, 2019). The only superficial runoff from the pro-glacial lakes is the Svínafellsá river at the western end of the southern lake at about 100 m a.s.l.

Svínafellsjökull has eroded a deep, 6 km long subglacial trough with its lowest point at an elevation of ca. 200 m below the present-day sea level and it has a maximum ice-thickness of ca. 500 m (Magnússon *et al.*, 2012). In February 2013 a debris avalanche with a volume of ca. 5.3×10^6 m^3 fell onto the southern lateral margin of the glacier covering an area of ca. 1.7 km^2 (Figure 1) (Ben-Yehoshua *et al.*, 2022). The debris is insulating the glacier ice below and had created a more than 40 m high offset between the debris covered part and the debris-free glacier by 2022. The source area of this debris avalanche was a sediment draped slope located below the steep northeastern face of Skarðatindur above the retreating tongue of Dyrhamarsjökull glacier. The debris avalanche deposit is being transported down-glacier with the ice-flow by about 120 m/yr (Ben-Yehoshua *et al.*, 2022). Another active rockslide of about 10^6 m^3 has been documented at the toe of Hrútsfjall above the northern lateral margin of Svínafellsjökull (Figure 1) (Ben-Yehoshua *et al.*, 2022).

At the end of the LIA Svínafellsjökull and the neighboring Skaftafellsjökull outlet glacier to the northwest merged west of Mt. Hafrafell (Hannesdóttir *et al.*, 2015; Guðmundsson *et al.*, 2019). The end moraine of Svínafellsjökull is considered a composite moraine and reaches up to 46 m above its surrounding terrain whereas the moraines of the neighboring glaciers Skaftafellsjökull and Morsárjökull reach a maximum height of 14 m (Lee *et al.*, 2018). Sedimentological analysis showed a higher amount of angular clasts, fewer striations, higher textural variability and a greater variability in landform height suggesting comparatively more supraglacial and/or englacial sediment input than at adjacent moraines at Morsárjökull, Skaftafellsjökull, Falljökull and Virkisjökull (Thompson, 1988; Everest *et al.*, 2017; Lee *et al.*, 2018). This indicates that the Svínafellsjökull valley has experienced more landslide activity than other nearby glacial valleys.

The distribution of permafrost around Öræfajökull is poorly understood. Permafrost modelling has predicted either sporadic permafrost (Obu *et al.*, 2019) or no permafrost (Czekirda *et al.*, 2019) in the uppermost part of the research area.

In 2014, a ~100 m long fracture was discovered on Svarthamrar, south of Svínafellsjökull, and in 2018, a much more extensive fracture system, cutting the entire northern mountain slope was identified (Sæmundsson *et al.*, 2019). A monitoring network was established and a halt of tourism activities on the popular glacier and a temporary stop of infrastructure development in the Freysnes settlement was decided (Matti and Ögmundardóttir, 2021).

The appearance of extensive deformation features at this slope sparked a larger monitoring and research project. To better understand the development of the site we present the initial assessment of the Svarthamrar slope instability, including morphological analysis, glacier changes and monitoring data. It will be followed by investigations of detailed structural geology and assessment of slope stability in a coming study.

METHODOLOGY

UAV surveys

Five Unmanned Aerial Vehicle (UAV) surveys were carried out in the study area (Figure 2). In 2016 (Ben-Yehoshua, 2016) and 2017 about 0.1 km^2 over the highest part of the fracture was mapped with a custom built hexacopter UAV with a Sony QX1 camera. Flight tracks were prepared with the MissionPlanner software. Five ground control points (GCPs) were distributed in the mapping area (Figure 2) and measured with survey grade GNSS rover and corrected with the continuous GPS base station in Skaftafell. The resulting average Ground Sampling Distance (GSD) of the imagery is 2×2 cm. In 2018 the western part of the study area was surveyed with a 3DR Solo UAV and the Sony QX1 camera. About 0.6 km^2 was mapped with an average GSD of 5×5 cm and 5 GCPs (Ben-Yehoshua and Gunnarson, 2018).

A large-scale UAV-based photogrammetric survey (with a DJI Mavic 2 Pro) was carried out in the summer of 2020 to map geological and geomorphological features. In August 2022 a UAV survey of adjacent Hvannadalur valley using the same hardware was added to the dataset. In total 3580 photographs from 24 flights were included in the processing. Steep parts of the research area were mapped by manual flying, making sure image overlap was sufficient and the remaining area was surveyed with preprogrammed flights with the Universal Ground Control Software (UGcS). The total mapped area covers 6.2 km^2 with an average GSD of 5×5 cm. Ground control was achieved by marking the locations of GNSS survey points in the UAV imagery (Figure 2). The processing software (Pix4D) estimated an accuracy of the data as given by a mean RMS error of 0.187 m based on the GCPs. The outputs include an orthoimage, a digital elevation model (DEM) and a 3D mesh. An interactive interface to view the 3D mesh is available at: https://v3geo.com/model/471. These data were used to map and identify features especially in the steep parts of the mountainside which are usually dark due to shadows on aerial and satellite imagery.

Morphological mapping and feature identification

The morphological mapping was conducted mostly with the 2020 UAV imagery and 3D mesh. Ground truthing of most sinkholes and bedrock fractures was conducted during fieldwork in the summers 2021 and 2022. Single round or elliptic sinkholes were marked with one marker (colored plus-signs). Linear sinkholes were mapped by two of the same markers at each end of the sinkhole. In some cases, a linear depression is visible on the surface with multiple smaller sinkholes inside. In this case every small sinkhole was identified with a marker. In some cases, a bedrock-fracture is visible at the bottom of a sinkhole. In these cases, both a bedrock-fracture and sinkhole were mapped. Sinkhole ages were mapped using imagery outlined in Table S1 and Figure 2. Bedrock fractures were traced where they were exposed and

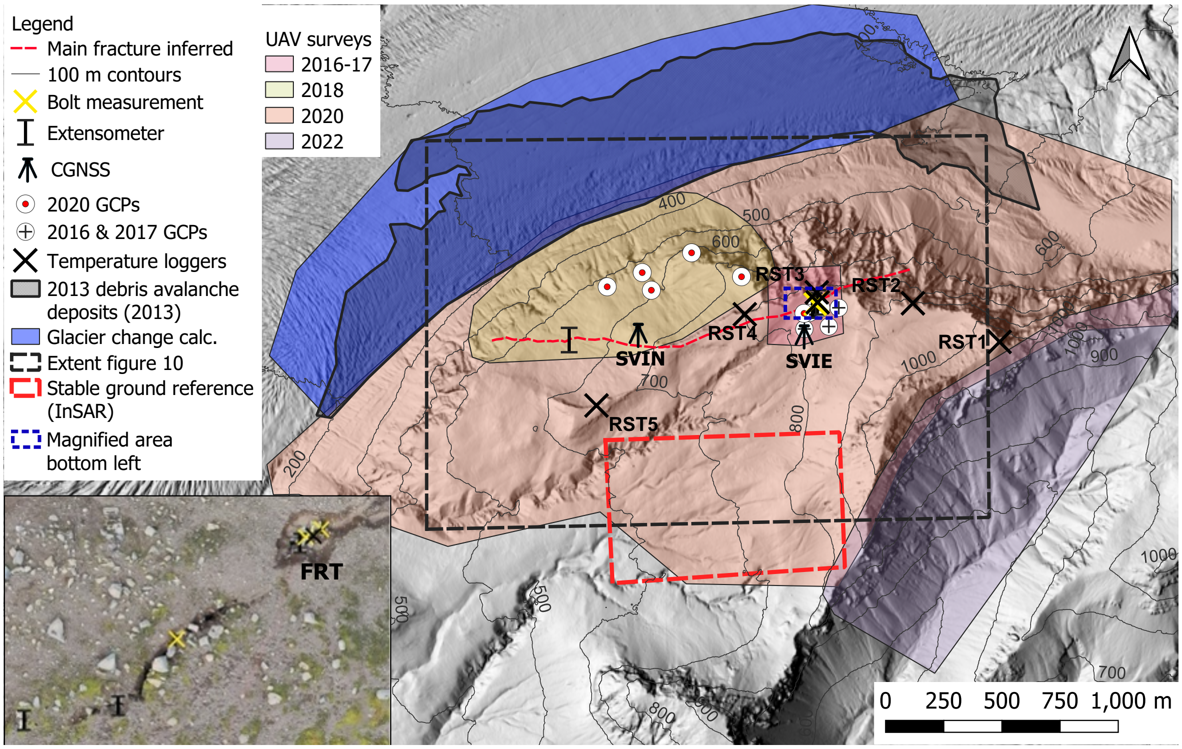

Figure 2. Map of the study area showing the inferred location of the main fracture and installed instrumentation. Areas surveyed by UAV since 2016 are illustrated by colored polygons. The blue polygon refers to the glacier area considered for thinning and ice-mass calculations. CGNSS refers to the continuous GNSS stations. Basemap: ÍslandsDEM, LMÍ. – *Kort af rannsóknarsvæðinu sem sýnir legu sprungunnar og mælibúnað. Svæði könnuð með flygildum frá árinu 2016 eru sýnd með lituðum flákum. Bláa svæðið sýnir þann hluta jökulsins sem er tekinn með í útreikningum á þynningu jökulsins og þyngd hans. CGNSS táknar samfelldar GNSS landmælingastöðvar. Grunnkortið er frá Landmælingum Íslands.*

showed an opening or were filled with loose superficial material. Minor jointing in effusive volcanic rock such as columnar joints and interlocking blocks were disregarded in this study as they are too abundant. Where multiple sinkholes and bedrock fractures clearly lined up, an underlying fracture was inferred along those features to get a better understanding of the bedrock fracturing of the slope. Marked inferred fractures are purely interpretive. The head scarp of the 2013 debris avalanche and the extent of its deposits are based on Ben-Yehoshua *et al.* (2022). Accumulations of rock fall deposits are marked as talus and fluvial deposits as alluvia fans.

Sinkhole age determination

To determine the minimum age of sinkholes, different aerial- and satellite imagery (Table S1) as well as ground-based imagery were compared. Note that the described sinkhole ages do not represent their actual age, but the dataset in which the respective sinkholes were first observed. Small features might not have been visible in 2009 and 2012 satellite data but in 2020 UAV imagery due to a higher spatial resolution. Furthermore, the high-resolution UAV data from 2016, 2017, 2018 and 2022 do not fully cover the research area (Figure 2), which might lead to features being recorded later despite their older actual age. Cumulative sinkhole numbers were counted from manned aircraft- and satellite derived imagery (1968, 1980, 1994, 2003, 2009, 2012, 2013, 2017 and 2021) and exclude sinkholes exclusively visible on UAV imagery. This is due to the temporal bias the large amount of small sinkholes mapped from the high-resolution UAV imagery (57) would create. Due to a gap in vertical imagery between 2003 and 2009, ground-based imagery was compared with the 3D mesh at similar view angles to constrain the time-frame of sinkhole evolution further.

Glacier thinning and glacier load on the subglacial slope.

To calculate the cumulative ice-mass loss an area of about 1.8 km^2 stretching to the approximate boundaries of the Svarthamrar slope instability to the centerline of the glacier was considered (blue polygon in Figure 2). In this area, the mean elevation change of 11 DEMs (Table S1) with respect to the 1890 glacier elevation (Hannesdóttir *et al.*, 2015) were calculated.

The load of the glacier on the subglacial slope was calculated for the same elevation data considering the subglacial topography from Magnússon *et al.* (2012) and an average ice density of 0.9 t/m^3 for ablation zones of temperate glaciers (Cuffey and Paterson, 2010). The source volume of the 2013 debris avalanche was calculated to be 5.3×10^6 m^3 (Ben-Yehoshua *et al.*, 2022). Based on the results from that study we estimated that about 95% of the 2013 debris avalanche deposits were deposited on Svínafellsjökull. Since the 2013 debris avalanche deposits consist to a large part of moraine and talus material, we applied the density of 2.37 t/m^3 for wet, coarse, mixed glacier till (Böðvarsson, 2004) as an estimate for the maximum density of the debris avalanche deposit. According to these parameters the weight of the debris avalanche deposit on the glacier is about 12.16×10^6 t. This weight was added to the glacier load on the subglacial slope in 2013.

Monitoring equipment

The established monitoring network is illustrated in Figure 2. In September 2016 three pairs of copper bolts were mounted into bedrock on both sides of the uppermost part of the fracture at 850 m a.s.l., establishing three measuring survey lines across the fracture (yellow X in Figure 2). The distance between the bolt pairs was measured with a steel measuring tape. After the discovery of the full extent of the fracture two continuous global navigation satellite system (CGNSS) stations (Septentrio PolaRX5) were installed in July 2018. One station (SVIE) is located at around 850 m a.s.l. SSW from the uppermost part of the main fracture. This location was chosen as it was considered to be outside of the active part of the slope. The other station (SVIN) is located, at around 650 m a.s.l., just north of the main fracture. These locations were specifically chosen to measure the movement along the fracture. Three extensometers (RST Instruments - Vibrating Vire Crackmeter) were installed on the uppermost part of the fracture at 850 m a.s.l. (two in September 2018, and one in August 2019) (Figure 3b). One additional extensometer was installed at the lower part of the fracture around 550 m a.s.l. (Figure 3d) in August 2019. The CGNSS and the extensometers are powered from batteries which are charged through solar panels. Due to a lack of solar power and storm damage to the antenna the CGNSS measurements have been interrupted every winter since 2018. The CGNSS, extensometer and webcam equipment are run and maintained by the Icelandic Meteorological Office (IMO) in collaboration with the Institute of Earth Sciences, Univ. Iceland.

To get a better understanding of the thermal conditions on the mountain, five temperature loggers (Geoprecision M-Log 5W-CABLE) were installed at 10 cm depth in north facing, vertical bedrock cliffs along the slope (Figure 2) for rock surface temperature (RST) measurements. For the season 2021-2022, data from only four RST loggers was retrieved. One temperature logger of the same type was lowered into the fracture at 850 m a.s.l. to a depth of about 8 m. The presented RST logging data spans the timeframe from August 28th, 2020 to September 28th, 2022.

InSAR analysis

The InSAR analysis was performed using the small baseline subset (SBAS) method for processing of four Sentinel-1 tracks from 2015 to 2022: two ascending and two descending. Interferograms of all image pairs possible from one snow free season to the

Figure 3. CGNSS stations and extensometers which were installed on the upper part of the fracture in 2018 and 2019. a) The CGNSS station SVIE, SSW of the upper part of the fracture at around 850 m a.s.l.. b) Extensometer located on the upper part of the fracture at 850 m a.s.l., installed in 2018. c) Extensometer located at the upper part of the fracture at 850 m a.s.l., installed in 2019 (photo: Ragnar Þrastarson 2019). d) Extensometer located on the lower part of the slope installed in 2019. Note the thickness of the sediments covering the bedrock in c) and d). – *CGNSS stöðvar og togmælar sem settir voru upp á efri hluta sprungunnar 2018 og 2019. a) Samfellda GNSS landmælingastöðin SVIE er staðsett SSV af efri hluta brotsins, í um 850 m hæð. b) Færslunemi á efri hluta sprungunnar í 850 m hæð settur upp árið 2018. c) Færslunemi á efri hluta sprungunnar í 850 m hæð settur upp árið 2019 (ljósmynd Ragnar Þrastarson 2019). d) Færslunemi í neðri hluta hlíðarinnar settur upp árið 2019. Athugið þykkt setlaga sem þekja berggrunninn í c) og d).*

next were produced, plus the next two consecutive interferograms (Table S2). Before 2015 no useable Sentinel-1 data was available. Standard geometric terrain corrections were applied (Meyer, 2019) using the ÍslandsDEMv1 elevation model (LMÍ). Interferogram stacks were produced using the InSAR Scientific Computing Environment (ISCE2) (Rosen *et al.*, 2012) and near-east and near-up deformation signals were extracted as described in Drouin and Sigmundsson (2019). Average velocity fields were extracted for the period 2015–2017 and 2017–2022 based on the detected deformation signal.

CGNSS baseline processing

The CGNSS data were analyzed using the GAMIT/GLOBK software version 10.7 (Herring *et al.*, 2016). The analysis was in the ITRF2008 reference frame (Altamimi *et al.*, 2012). SVIE was installed south of the fractured area and is consid-

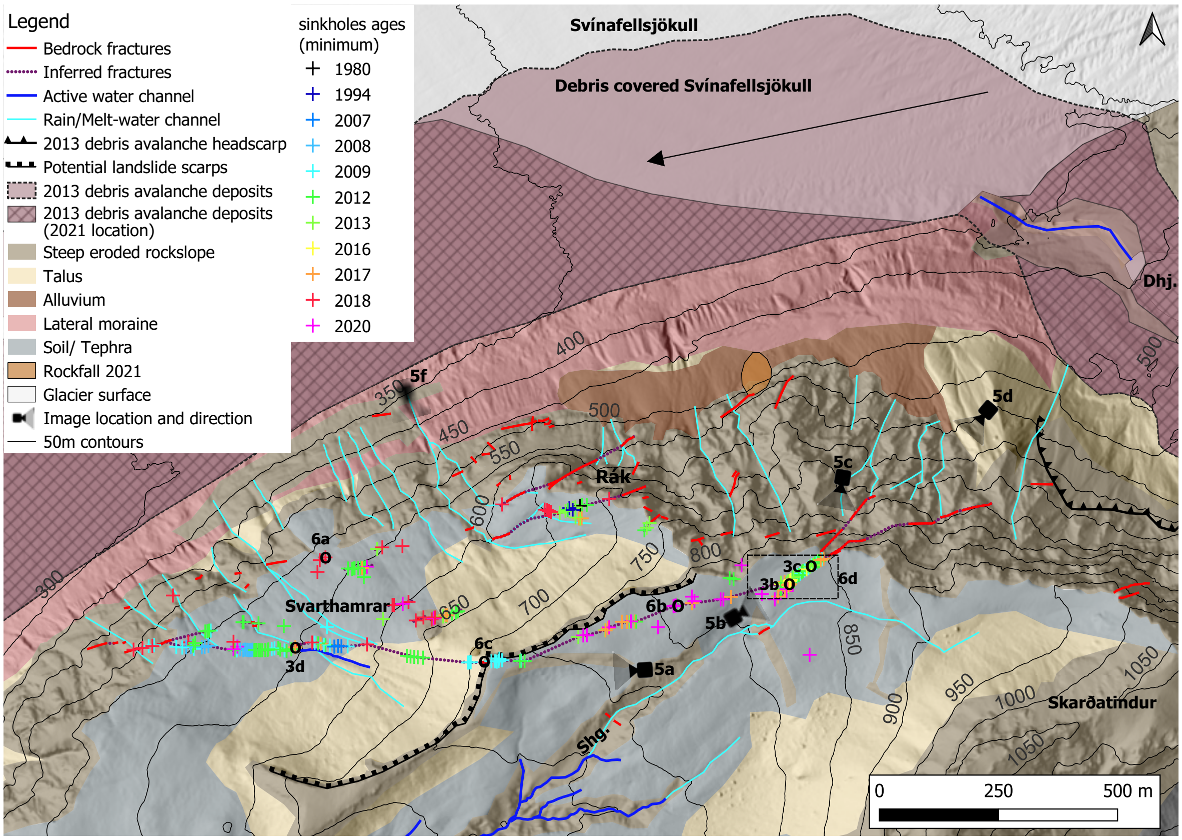

Figure 4. Geomorphological map of the research area. Note the 2013 debris avalanche deposits are moving past the slope with the glacier flow indicated by the black arrow. Image locations are shown by black circles, a dashed, black box and camera symbols with the respective figure number. Shg. Svarthamragil; Dhj. Dyrhamarsjökull (debris covered). The hillshade DEM is from Jóhannesson *et al.* (2013). – *Landmótunarkort af rannsóknarsvæðinu. Athugið að skriðuefnið frá 2013 færist meðfram fjallshlíðinni (sýnt mað svartri ör). Staðsetningar mynda eru sýndar með hringjum eða myndavélartáknum með viðkomandi myndnúmeri. Shg. Svarthamragil; Dhj. Dyrhamarsjökull (hulinn skriðuefni). Grunnkort: fjall, 2020 flygildi DEM; jökulyfirborð, 2021. Hæðarlíkan Jóhannesson et al. (2013).*

ered to be on stable ground. SVIN is located north of the main fracture and thus within the deforming area. Daily positions were derived by averaging the measurements of the respective station over 24h. To get the most accurate estimate for movement of the slope, relative to its surroundings, we look at relative change in distance between the two stations. As the stations are located only 731 m apart, we effectively eliminate the regional effects (e.g., atmospheric effects, Plate tectonics and glacio-isostatic uplift) acting on both stations and reducing the signal to noise ratio significantly, by calculating the difference between daily coordinates of the two stations SVIN and SVIE. Then looking at the differential change of the coordinates over time we can track local deformation signals acting differently on the two stations. Sudden and gradual movement on the main fracture should show up in the differential time series. In addition, to further improve the ability to identify movement on the fault system, the coordinates have been rotated to match the approximate normal (330°) and parallel (240°) direction of the fault system. A rolling 40-day mean on the timeseries was estimated and datapoints falling outside of 2 standard deviation from the mean were classified as outliers and removed.

Temperature regression methodology

To assess the long-term temperature development of the area, a temperature time series from the Fagurhólsmýri weather station (FWS) (9 m a.s.l.), about 16 km to the southeast (Figure 1), was analyzed (data available at the IMO). The measurements at FWS date back to the year 1898. The correlation coefficient R^2 (Magnin *et al.*, 2015) between the daily measurements at FWS and the single RST stations during the overlapping timeframe (01.09.2020–01.09.2022) was calculated to be between 0.83 and 0.85 for all RST 1-4.

Linear regression models were fitted for FWS and the single RST stations on site. The resulting slope and intercept were then applied to back-calculate temperature values for the RST logger locations with (1):

$$RST = FT \star m + b \tag{1}$$

Where RST is the back calculated temperature, FT is the measured temperature at FWS, m is the slope from the respective linear regression, and b is the intercept from the linear regression.

RESULTS

Slope morphology and the signs of instability

The northern slope of Svínafellsfjall was glacially overprinted during the LGM and no post-LGM volcanic deposits (except for tephra) could be mapped. The slope itself is at the former confluence of two glaciers, south of Svínafellsjökull and west of Dyrhamarsjökull (Figure 1). Having been eroded by glaciers from two sides the general slope shape is protruding towards the north which resulted in most slopes in the study area to either face northwest or northeast (Figure 4). Northwest-facing slopes are usually moss covered, plateau-like, gently sloping with occasional lava layers forming steps, and covered in soil, tephra, or talus deposits. A layer of effusive volcanic rock that runs through the area forms two northwest facing, cirque-like bowls (Figures 4 and 5a,f) hanging 200–250 meters above the glacier surface. The crown of the western bowl is circular whereas the crown of the eastern bowl is more undulating. Each bowl covers an area of about 0.2 km^2 and has a vertical or near vertical cliff at the top. The area below gradually changes from about 35°–40° steep talus to a gentler 10°–20° slope at the bottom of the bowl. The height from the bottom to the top cliff of the hanging bowl is about 200 m. The bowls are characterized by talus that accumulated below the cliffs.

Svarthamragil is the largest canyon in the study area, with a length of about 2 km and in parts more than 50 m depth. It eroded into the west facing plateau with a creek running through it roughly from northeast to southwest. The westernmost 500 m of the canyon is dry during the summer months. Looking from west to east up Svarthamragil canyon (Figure 5e), the slope shape from Skarðatindur in the south to the plateau in the north forms a half-U-shaped valley that ends abruptly at the northeastern cliff towards Dyrhamarsjökull. However, towards the northeast the plateau-like area ends abruptly (Figure 5b,c,d) and turns into steep eroded rock slopes. These northeast-facing rock slopes consist mostly of steep eroded layers of effusive lavas and tuffacious rocks. Often the bare bedrock is exposed and sometimes the slopes are covered in talus and/or vegetation. They are cut by numerous canyons that eroded almost vertical cliffs into the slope and formed steep bedrock ridges between each other. Below Skarðatindur, a nearly vertical part of the northeast-facing cliff lies the headscarp and depletion area of the 2013 debris avalanche (Figure 4). Most of the debris avalanche was deposited on the Svínafellsjökull glacier surface and has since moved about a kilometer west with the glacier flow since their deposition (Ben-Yehoshua *et al.*, 2022). Talus slopes throughout the study area vary from being very fresh and unvegetated to covered in moss and seemingly inactive. Between October 2020 and August 2021 a rockfall occurred at the bottom of the steep eroded slope northeast of Rák (Figure 4). The top of the lateral moraine in Figure 4 is about 100 m above the present-day glacier surface.

A total of 214 sinkholes (Figure 6a,b) and bedrock fractures (Figures 5c,d and 6c) were mapped in the

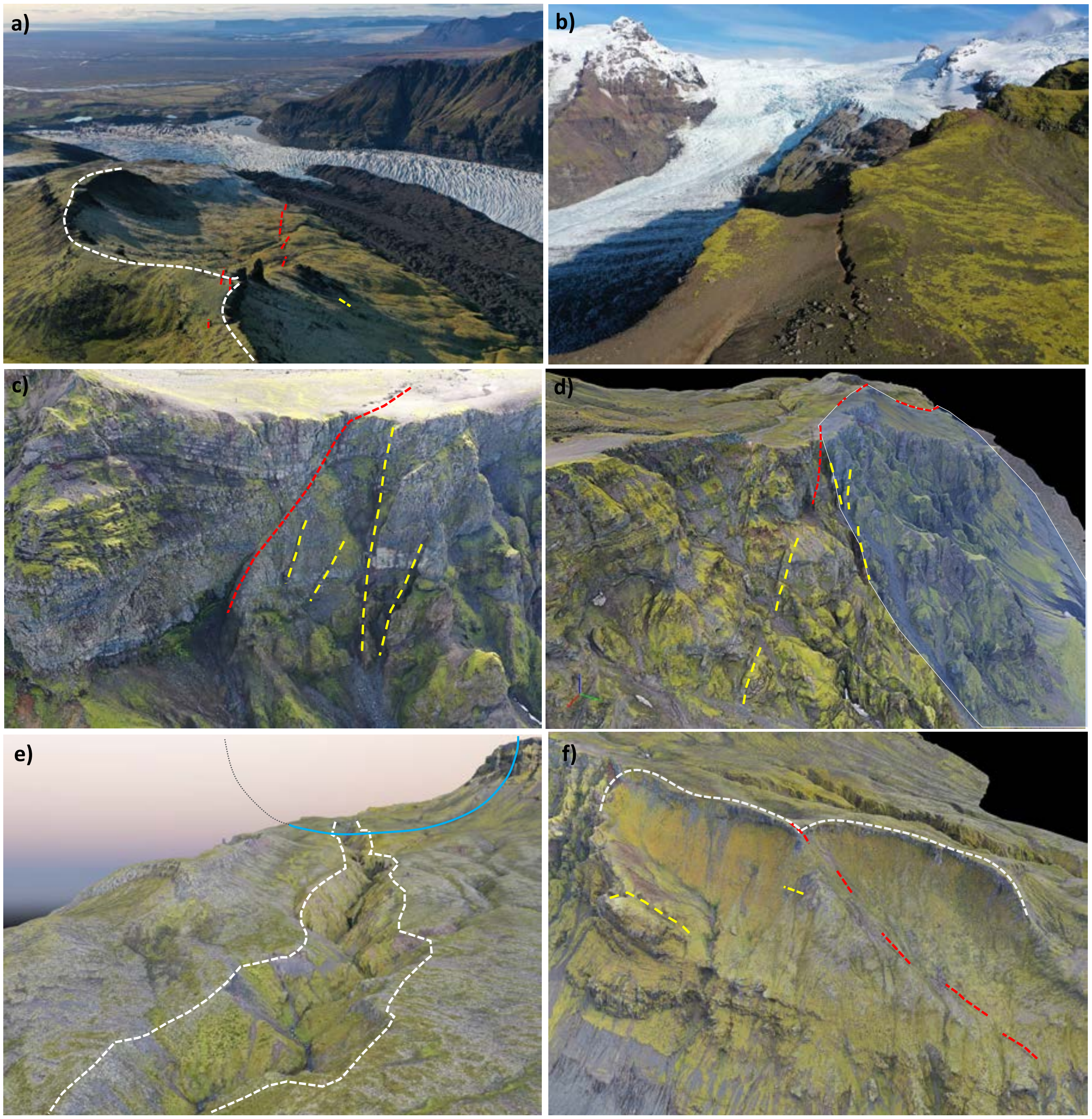

area. The southernmost, and longest alignment of these features can be traced for about 1950 m from the west at 400 m a.s.l. up to 850 m a.s.l. and down to 730 m a.s.l. at the eastern end (Figure 4), defining an area of about 0.9 km^2 between the fracture to the south and the glacier to the north. The westernmost part of this alignment runs through tuffaceous breccias and effusive lavas and shows a number of slightly offset bedrock fractures in the cliffs right above Svínafellsjökull. When the fracture reaches the vegetated, soil covered and less steep part of the mountainside at about 480 m a.s.l. it is characterized by numerous aligned, linear sinkholes of lengths between 0.2 m and 100 m, up to 5 m wide, and clearly visible in aerial im-

Figure 5. Overview images of the main fracture features. Dashed red lines indicate features of the main fracture whereas yellow dashed lines show locations of secondary fractures a) UAV image looking west onto the lower part of the fracture above Svarthamrar in E-W (90-270°) direction. Elongated sinkholes and bedrock fractures can be traced down the slope. White dashed lines illustrate the top of the rounded cliffs forming cirque-shaped bowls. The extent of the 2013 debris avalanche deposits is visible on the glacier and so is the northern pro-glacial lake (image taken 2019). b) UAV image looking towards the east onto the uppermost part of the fracture at about 850 m a.s.l. The surface expression of the fracture is about 110 m long and 2 m wide in the picture (image taken 2019). c) UAV image looking onto the same fracture feature from north to south. Multiple discontinuities can be traced cutting through different layers in the cliff (image taken 2020). d) 3D mesh scene looking towards the west along the main part of the Svarthamrar slope instability. The left linear discontinuity from c) can be traced further down the slope and forms a lineament that strikes east-west and dips about 80° to the south. A more vertical discontinuity can be traced about 100 m further down-slope. A potential minimum area of the slope is highlighted as blue transparent polygon. e) 3D mesh scene looking west, up Svarthamragil canyon (sides of the canyon are marked with white, dashed lines), towards Skarðatindur on the right side of the image. A blue line indicates the half eroded U-shaped valley geometry, and the thin black line indicates a hypothetical continuation of an earlier glacial valley shape. f) 3D mesh scene looking south towards two hanging bowls (edge of the upper cliff are marked with white, dashed lines). Major sinkholes are marked with red lines. Panels d) e) and f) are taken from the 3D mesh. – *Yfirlitsmyndir af helstu sprungukerfunum. Rauðar brotalínur tákna aðal sprungukerfið en gular brotalínur sýna aðrar sprungur. a) Horft til vesturs á neðri hluta sprungunnar fyrir ofan Svarthamra í austur-vestur átt (90–270°). Niður hlíðina má rekja ílöng jarðföll og sprungur. Hvítar strikalínur efst á klettabeltunum sýna hringlaga skálamyndanir. Umfang skriðuefnisins frá 2013 sést á jöklinum og norðurhluta jökullónsins. Mynd frá 2019. b) Horft til austurs á efsta hluta brotsins í um 850 m y.s. Sprungan er sýnileg á um 110 m bili á yfirborði. Mynd frá 2019. c) Horft á sömu sprungu frá norðurs til suðurs. Hægt er að rekja margar ósamfellur (stökkar línur) sem skera mismunandi lög í klettinum. Mynd frá 2020. d) Horft til vesturs meðfram meginhluta óstöðugu fjallshlíðarinnar. Vinstri línulega ósamfellu frá c) má rekja neðar í hlíðinni og myndar hún þar línu með austur-vestur stefnu. Lóðrétta ósamfellu má rekja um 100 m neðar í hlíðinni. Hugsanlegt lágmarksumfang fláabrots er merkt sem blár gagnsær marghyrningur. e) Horft til vesturs, upp Svarthamragil (hlíðar gilsins eru merktar hvítum strikuðum línum), í átt að Skarðatindi hægra megin á myndinni. Bláa línan sýnir hálf-U-laga lögun dalsins og þunna svarta línan gefur til kynna ímyndað framhald af fyrra jökuldalsformi. f) Horft til suður í átt að tveimur hangandi skálum (brún efra klettabeltisins er merkt með hvítum strikuðum línum). Helstu jarðföll eru merkt með rauðum línum. Myndir d) e) og f) eru úr 3D líkani.*

agery (Figure 5f). At 550 m a.s.l. a bedrock fracture can be observed as a near-vertical joint of about 35 cm width (Figure 3d), striking at about 45° azimuth with a minimum depth of 11m (plumb line measurement). At this location a small active water channel drains into the fracture. At about 700 m a.s.l. the lithology changes from tuffaceous breccia to intermediate lavas (Helgason and Duncan, 2013) which form a 25 m high, steep rock slope. The layer consists mostly of tightly interlocking blocks and is the same lava layer that forms the top steep part of the earlier described bowl like features (Figure 5a and f). Where the alignment of sinkholes intersects with this lava layer, a vertical crack filled with rock fragments can be observed (Figure 6c). Around this location the strike of the aligned sinkholes of the strike of the main fracture changes from 93° to the west to 73° towards the east.

The top of this lava layer forms a gently west sloping plateau, covered with soil of varying thickness. Continuing east, sinkholes of up to 5 m length occur irregularly along the lineament (Figure 4). The line of sinkholes can be traced for about 600 m to the east until reaching a pronounced line of sinkholes at 840 m a.s.l., which runs to the highest point of the fracture to the edge of the cliff (Figure 5b). Where the sediment cover is only 10–30 cm thick a 30–40 cm wide bedrock joint can be observed following the pre-existing discontinuities in the bedrock to form a linear fracture (Figure 3b,c). The minimum depth of one of

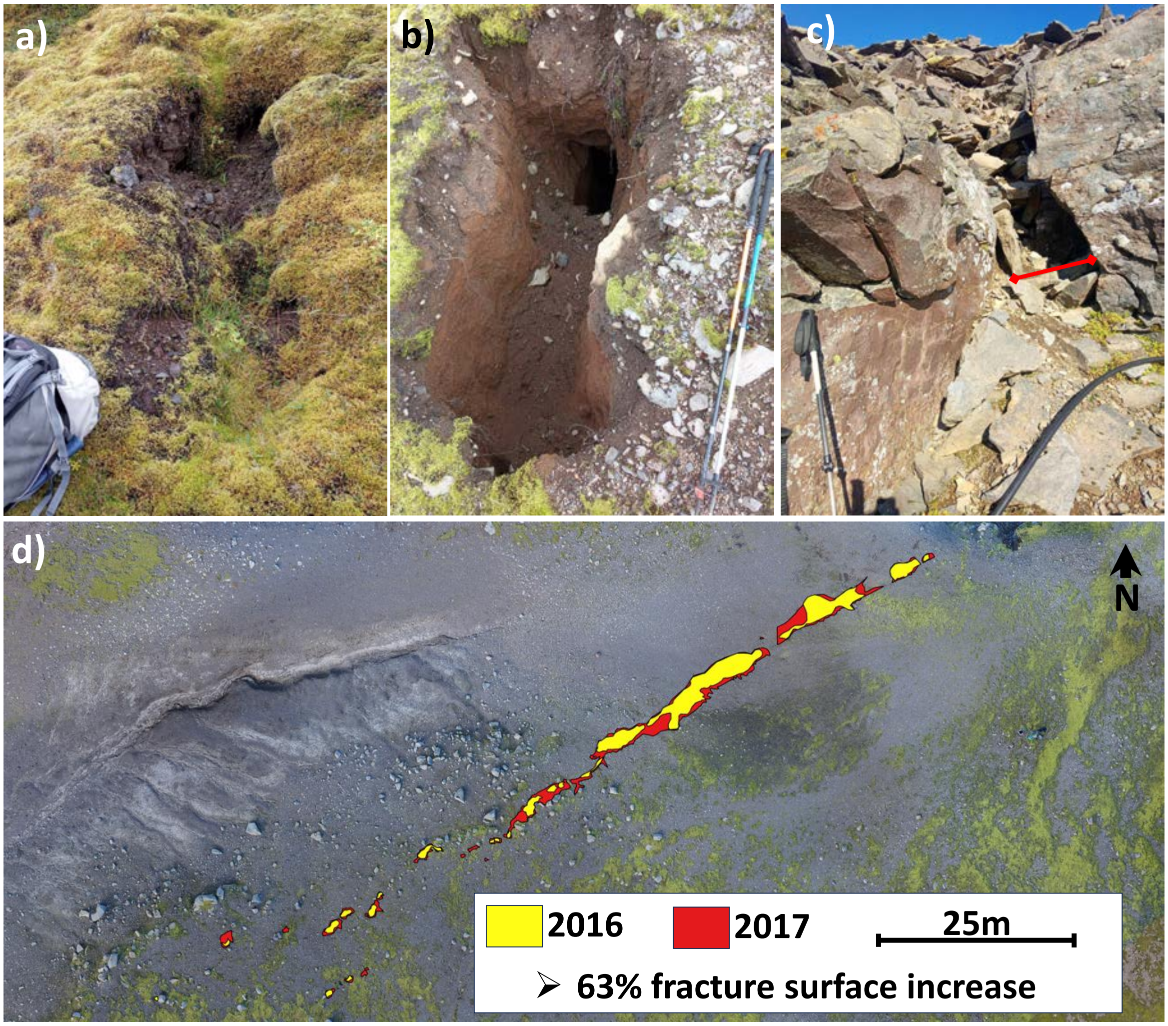

Figure 6. a) A small inactive looking sinkhole; old moss is preserved, and new grass started to grow (backpack for scale). b) A more pronounced recently active sinkhole. At the bottom the bedrock fracture can be seen (hiking poles for scale). c) A 40 cm wide (red line) vertical bedrock joint filled with debris, at the continuation of the main fracture in a bedrock cliff (hiking pole for scale). d) Changes in the extent of the surface expression of a part of the main fracture between 2016 and 2017. See Figure 4 for image and map locations. (Basemap: 2017 UAV survey). – *a) Lítið, óvirkt jarðfall; gamall mosi er varðveittur og nýtt gras byrjað að vaxa (bakpoki sem mælikvarði). b) Meira áberandi nýlegt, virkt niðurfall. Neðst má sjá sprunguna í berggrunni (göngustafir sem mælikvarði). c) 40 cm breið (rauð lína) lóðrétt sprunga í berggrunni fyllt með lausagrjóti sem sést í framhaldi af sprungu í klettabeltinu (göngustafur sem mælikvarði). d) Breytingar á stærð á sýnilegri aðal sprungunni milli 2016 og 2017. Staðsetningar mynda og kortsins sýndar á 4. mynd. (Grunnkort: 2018 drónamynd).*

these fractures was measured to 8 m using a plumb line. Only horizontal and no vertical offset was observed on the fractures (Figure 3b,c,d). The uppermost part of the main fracture, surveyed by UAV in 2016 and 2017, shows clear growth of its surface expression (Figure 6d) between those years. However, between 2018 and 2020 this fracture did not grow significantly. East from there, two discontinuities can be traced vertically through an 80 m high cliff on the opposite slope, consisting of subaerially erupted lavas, tuffaceous breccia and sedimentary rocks, forming a clear discontinuity (Figure 5c,d). Further down to 730 m the trace of the surface expression of the main fracture is lost under talus (Figure 4). Continuing the lineation about 100 m to the northeast another bedrock fracture can be seen further east entering the head scarp of the 2013 debris avalanche.

Downslope (north) from the main fracture numerous sinkholes of varying sizes occur, aligned in rows or as single holes (Figure 4). Some of the sinkholes look fresh and show recent collapse of sediment from the margins (Figure 6b) whereas others look less active with some vegetation starting to grow in the depression (Figure 6a). Up to 1.5 m thick soil and tephra lies on parts of the west facing plateau. The soil surface between aligned sinkholes is often unaffected by collapse structures even though a bedrock fracture clearly lies underneath (Figure 3d).

The age of main fracture

The first sinkhole is visible next to the cliff called Rák (Figure 4) in 1980 aerial imagery but not visible in 1968 imagery. Several additional sinkholes appeared nearby by 1994, forming a E-W lineation. No additional changes were detected in 2003 imagery.

There is a data gap in high-resolution aerial/-satellite imagery between 2003 and 2009. In the 2009 QuickBird2 panchromatic imagery (GSD 0.6×0.6 m) elongated sinkholes are clearly visible in the western part of the study area (same area as in Figure 5a,f) and aligned but isolated sinkholes at the uppermost part of the fracture (same area as Figure 5b and 6d). Those features had grown significantly in 2012, and further in 2013 and 2017. During fieldwork in 2016 and 2017 the sinkhole surfaces in the uppermost fracture appeared freshly collapsed and changes between these two years were clearly visible (Figure 6d) and were most likely produced by continuous collapse of soil into the fracture as well as growth of the fracture during this year. Numerous new sinkholes were identified across the entire slope in 2017 aerial imagery especially in the plateau between the uppermost fracture (Figure 5b) and the elongate sinkholes in the lower plateau (Figure 5a). Many more small sinkholes have been mapped across the slope with the high-resolution UAV imagery and ground truthing. The photograph in Figure 7b was taken in 2008 from the ring road at Skaftafell about 7 km northwest from the study area. Despite the distance it allows a good view of the lower part of the main fracture. Linear features 8, 9 and potentially feature 10, can be identified in both Figures 7a and 7b. This shows that the elongated fracture features in this area were already developed by 2008. The image for Figure 7d was taken in 2007 from the Svínafellsjökull glacier surface towards southeast. The largest sinkhole on the slope (feature 8) is still identifiable as a dark dot when compared with Figure 7c. Features 9 and 10 are not visible in Figure 7d, which is likely due to the view angle of the photograph. However, we establish that a major sinkhole was visible on the slope by 2007. Even though a sinkhole on Rák was observed as early as 1980 it can be stated that the initiation of the main fracture formation occurred after 2003.

Glacier changes

Svínafellsjökull has lost a large volume of ice since the LIA maximum ca. 1890 (Hannesdóttir *et al.*, 2015). Here we present glacier surface elevations over a 131-year period and relate the changes to the evolution of the Svarthamrar slope instability. Figure 8 illustrates the glacier changes along a profile below the mapped Svarthamrar slope instability, including the bed, (Magnússon *et al.*, 2012) and the location of the main fracture in the profile. This view highlights that the upper part of the main fracture lies ca. 1000 m above the true valley floor, of which ca. 500 m is currently covered by glacier ice. Throughout the 131 years there were two phases of no or very limited thinning of the glacier. From about 1960 to 1994, and a stable phase from 2011 which is still ongoing at the time of writing. Between 1994 and 2011 almost 50 m of ice thickness was lost which corresponds to the reduction of about 45.9 tons/m^2 of loading on the subglacial slope (Figure 9). Between 2003 and 2007 numerous sink holes appear across the slope indicating the onset of deformation affecting large parts of the slope, (Figures 7 and 9) which is indicated by the vertical, light grey bar in Figure 9b. This timeframe coincides with the highest glacier thinning rates mea-

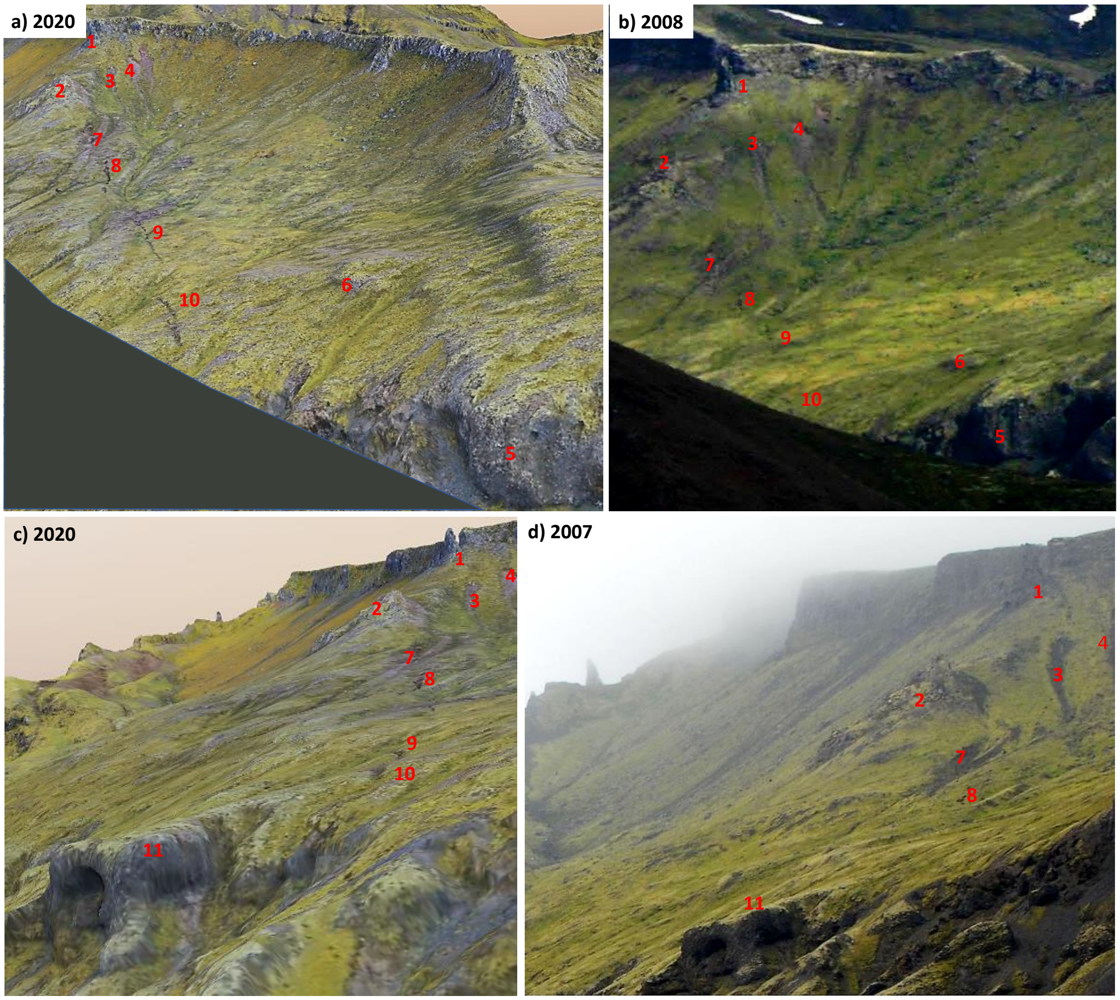

Figure 7. Comparison of different view angles of the 2020 3D-mesh on the left panels a) and c) with ground-based photography from 2008 (b) and 2007 (d) on the right panels. The capture locations of b) and d) are shown in Figure 1c). Recognizable features are numbered. 1 Prominent bedrock cliff; 2 bedrock outcrop on the slope; 3 gravel patch on slope; 4 gravel patch on slope; 5 cliff in lower part of the slope; 6 bedrock outcrop; 7 gravel patch in slope; 8 elongated sinkhole; 9 elongated sinkhole; 10 elongated sinkhole; 11 cliff of entablature lava. Distortion in the photographs compared to the 3D-mesh is due to the distance from where they were taken (several kilometers) and different focal lengths. Sinkholes 8, 9 and 10 are faintly visible in b) and sinkhole 8 is visible in d), 9 and 10 might be there but not visible from this angle. b) Photo by Steinar Sigurðsson in July 2008. d) Photo by Marco Weingaertner in August 2007. – *Samanburður á mismunandi sjónarhornum þrívíddarlíkans (2020) til vinstri á myndinni a) og c) við ljósmyndir 2008 b) og 2007 d) hægra megin. Myndatökustaðir b) og d) eru sýndir á mynd 1c. Þekkjanleg ummerki eru tölusett. 1 Klettasúla; 2 klettur í hlíðinni; 3 malarrák í hlíð; 4 malarrák í hlíð; 5 klettur úr hraunlögum; 6 klettur í hlíð; 7 malarrák í hlið; 8 ílangt jarðfall; 9 ílangt jarðfall; 10 ílangt jarðfall; 11 klettur. Bjögun í myndunum, miðað við þrívíddarnetið er vegna fjarlægðar frá þeim stað sem þær voru teknar (nokkrir kílómetrar) og mismunandi brennivídd. Jarðföll 8, 9 og 10 sjást lítillega á mynd b) og hola 8 sést í d), 9 og 10 gætu verið þarna en eru ekki sýnilegar frá þessu sjónarhorni. Ljósmynd (b): Steinar Sigurðsson, júlí 2008. Ljósmynd (d): Marco Weingaertner, ágúst 2007.*

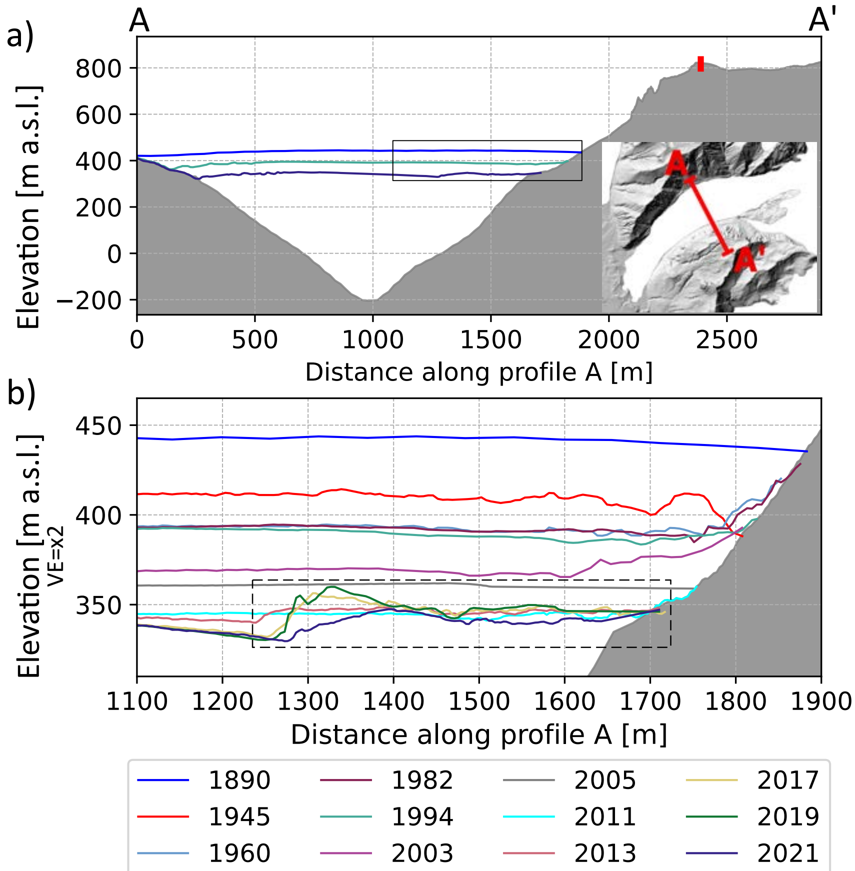

Figure 8. a) Cross section A-A' showing the glacier surfaces in 1890, 1994 and 2021 as well as the subglacial bed and the profile of the mountainside in grey. The red dot in the upper right indicates the location of the main fracture. The black box indicates the extent of Figure 8b. b) A shorter section along the same profile A-A'. Twelve glacier elevations are plotted showing the development over 131 years. Note the effect of the 2013 debris avalanche deposits on the elevation profiles in 2013, 2017, 2019 and 2021 (dashed black box). Panel b) has a vertical exaggeration (VE) of factor 2 to better illustrate the vertical glacier changes. – *a) Þversnið A-A' sem sýnir yfirborð jökulsins 1890, 1994 og 2021 ásamt jökulbotni og staðsetningu á sniði fjallshlíðarinnar í gráu. Rauði punkturinn sýnir staðsetningu meginsprungunnar og kassinn umfang myndar 8b. b) Styttri hluti af sama sniði A-A'. Teiknaðar eru upp 12 jökulþykktir sem sýna þróunina á 131 árs tímabili. Takið eftir áhrifum skriðufallsins 2013 á hæðarsnið áranna 2013, 2017, 2019 og 2021 (kassi afmarkaður með svartri brotalínu). Mynd b) hefur lóðréttar ýkjur (VE) 2 til að sýna betur lóðréttu jöklabreytingarnar.*

sured over the 131-year period (Figure 9). The deposition of the 2013 debris avalanche onto Svínafellsjökull is indicated by a dotted vertical line in Figure 9b. This insulated part of the glacier is currently located directly below the area of the Svarthamrar slope instability (Figures 1, 4 and 5a). The profiles of the years 2013, 2017, 2019 and 2021 in Figure 8b show that the debris covered part of the glacier stagnated since 2013 while the debris-free glacier continued to thin. By 2021 the debris cover has started to move out of the profile resulting in renewed lowering of the glacier surface. The weight added to the glacier by the 2013 debris avalanche deposits was calculated to be $\sim 12.16 \times 10^6$ t. This added to the load of the glacier

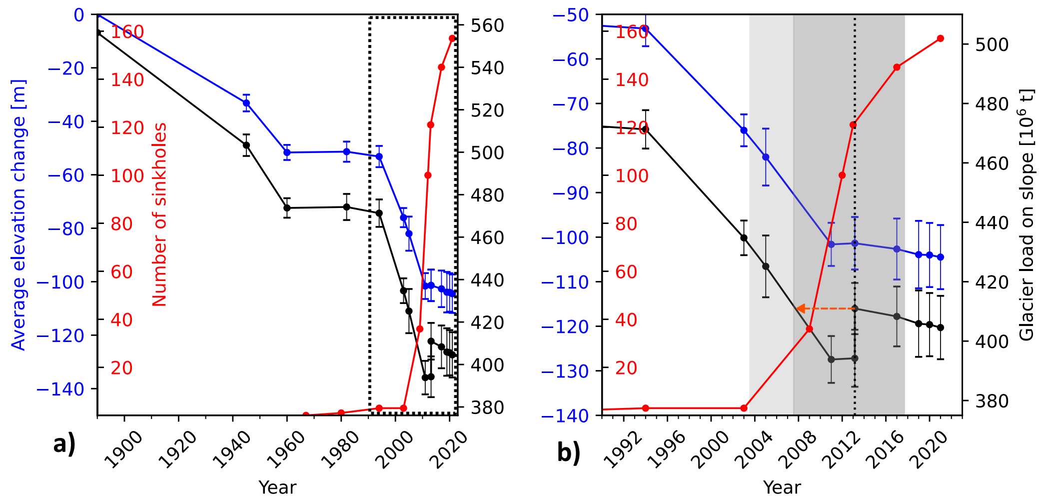

Figure 9. In both panels, a) and b), the left y-axes with blue graphs and numbers illustrate the cumulative mean elevation change in front of the Svarthamrar slope instability over the years shown on the x-axis. The change in glacier load on the subglacial slope is illustrated as black graphs which correspond to the right y-axis in both panels. The glacier area used for this calculation is indicated in Figure 2. The red graph and numbers in both panels indicate the cumulative sinkhole count visible on aerial- and satellite imagery. a) Covers the timeframe from 1890 to 2022. The dotted black box illustrates the magnified time series shown in panel b). b) The dotted vertical line indicates the occurrence of the 2013 debris avalanche. The orange arrow illustrates that the load on the slope right after the 2013 debris avalanche is equivalent to the glacial load in 2007. The vertical, light grey bar indicates the timeframe 2003–2007 when the main fracture formation was initiated, and the vertical, dark grey bar indicates the timeframe of slope deformation. – *Í a) og b) sýnir vinstri Y-ásinn uppsafnaða meðalhæðarbreytingu fyrir framan óstöðugu hlíðina við Svarthamra. Breyting jökulfargsins á hlíðina sem er undir jökli er táknuð með svörtum línum á hægri Y-ásnum. Svæðið á jöklinum sem notað er í þessum útreikningi er sýnt á 2. mynd. Rauða línuritið og tölurnar sýna uppsafnaðan fjölda jarðfalla sem sjást á loft- og gervihnattamyndum. a) Spannar tímabilið frá 1890 til 2020. Svarti kassinn sýnir tímaröðina á mynd b). b) Lóðrétta strikalínan sýnir skriðuna árið 2013. Appelsínugula örin sýnir að fargið á hlíðina eftir skriðuna árið 2013 er sambærileg við gildin árið 2007. Lóðrétta ljósgráa skyggða svæðið táknar tímann milli 2003 og 2007 þegar megnið af sprungumynduninni fór fram, og lóðrétta dökkgráa svæðið sýnir þann tíma þegar hlíðin aflagaðist.*

on the subglacial slope (Figure 9). The deposition of the 2013 debris avalanche reset the load at the foot of the Svarthamrar slope instability to 2007 values (indicated by orange arrow in Figure 9b).

Monitoring system and current observations

InSAR data shows a clear deformation signal in the slope north of the main fracture between 2015 and 2017 (Figure 10a,b). After 2017 no deformation is detected (Figure 10c,d). The near-east and near-up ground motion between 2015 and 2017 (Figure 10a,b) shows that the slope north of the main fracture seems to have deformed in two directions. Northwest of the main fracture the ground motion had an east-component of up to 10 mm/yr and a slight upward motion. Northeast of the fracture the ground deformation occurred as a west-component of 10–15mm/yr and a downward deformation of up to 20 mm/yr. The contact between those two segments starts were the main fracture takes a turn and then continues in a northeast direction.

Manual tape measurements at bolts installed on either side to the main fracture between 2016 and 2017 yielded a maximum opening of 16 mm between 2016

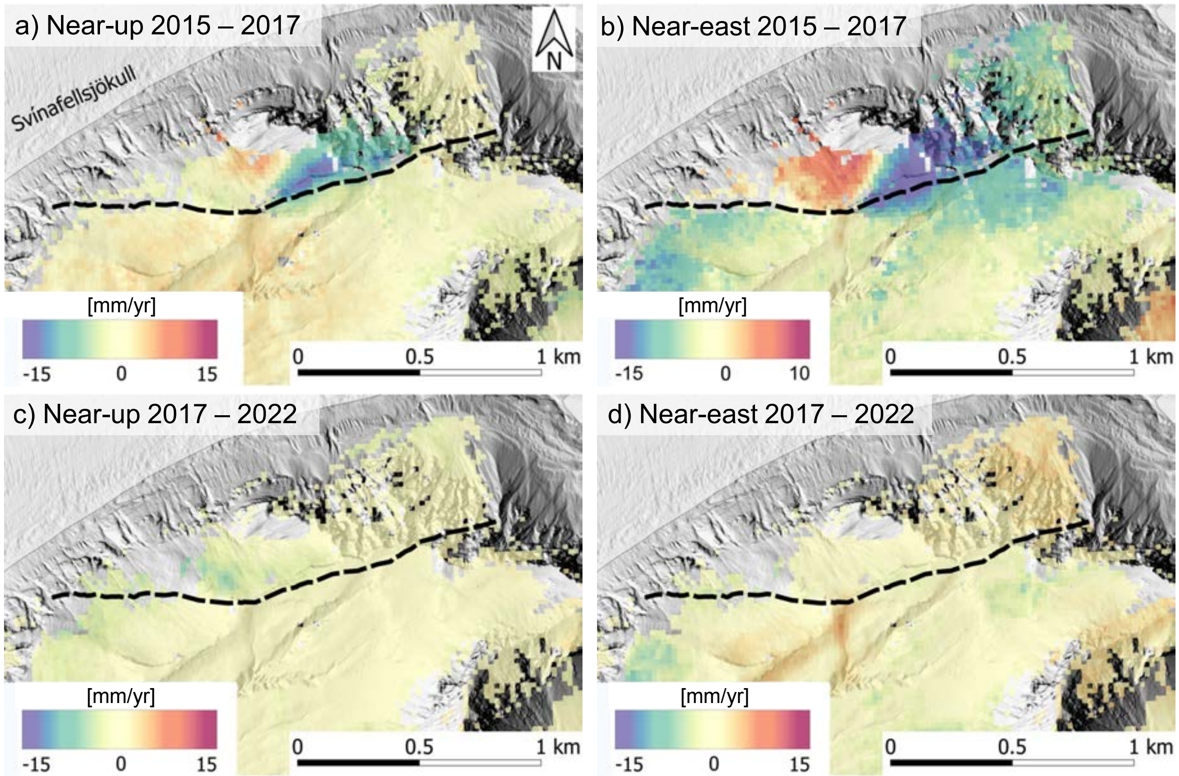

Figure 10. InSAR data showing near-up deformation 2015–2017 (a), near-east deformation 2015–2017 (b), near-up deformation 2017–2022 (c), and near-east deformation 2017–2022 (d). Scale bars represent displacement rate, blue/purple colors indicate downward (a and c) or westward movement (b and d), whereas orange/red colors indicate upward (a and c) or eastward movement (b and d). The dashed, black line in all 4 images indicates the location of the main fracture, and the glacier extent is marked with a white, transparent polygon. The extent of the areas shown in a)-d) is illustrated in Figure 2. Basemap: LMÍ – *InSAR gervihnattagögn sem sýna aflögun í nær-upp átt frá árinu 2015 til 2017 (a), aflögun í nær-austurátt frá árinu 2015 til 2017 (b), nær-upp aflögun frá 2017 til 2022 (c), og nær-austur aflögun frá 2017 til 2022 (d). Mælikvarðar neðst á myndunum sýna aflögunarhraða þar sem bláir/fjólubláir litir tákna hreyfingu niður (a og c), eða hreyfingu í vestur við (b og d), en appelsínugulir/rauðir litir tákna hreyfingu uppávið (a og c) eða austurhreyfingu (b og d). Svarta línan í öllum fjórum myndunum sýnir staðsetningu aðalsprungunnar. Jökullinn er táknaður með ljósbláum lit. Umfang svæðanna sem sýnd eru í a)-d) er sýnd á 2. mynd. Grunnkort frá Landmælingum Íslands.*

and 2018 in a north south direction across fractures (Table 1). Since 2018 a maximum widening of 6 mm has been measured at the bolts. This is in accordance with the extensometer data collected by the IMO which detected about 6 mm opening of the fracture since the installation in 2018. GNSS measurements (Figure 11) have shown no horizontal displacement and only about 8 mm lowering since the beginning of the measurement in July 2018. The total deformation detected at the main fracture since the installation of the monitoring network is less than a centimeter which would result in less than 3 mm/yr.

Temperature measurements and regression

Rock surface temperature was measured over a two-year period (Figure 12a) on north facing slopes at four locations at different elevations (Table 2). Tempera-

Table 1. Distance between each bolt pair and derived extension. Bolt pairs 1–3 were placed northeast to southwest, see Figure 2. Na. "not available". – *Bil og færslur á milli boltapara. Boltapör 1–3 liggja norðaustur til suðvesturs á 2. mynd. Na. engin gögn.*

year	2016	2017	2018	2019	2020	2021	2022
bolt pair	distance [cm]						
1	96.3	96.7	97.9	98.3	98.2		98.4
2	62.3	63.5	63.7				
3	76	77.3	76.5	76.6	76.5	76.6	76.6

period	2016–2017	2017–2018	2018–2019	2019–2020	2020–2021	2021–2022
bolt pair	extension [cm]					
1	0.4	1.2	0.4	-0.1	Na.	0.2
2	1.2	0.2	Na.	Na.	Na.	Na.
3	1.3	-0.8	0.1	-0.1	0.1	0

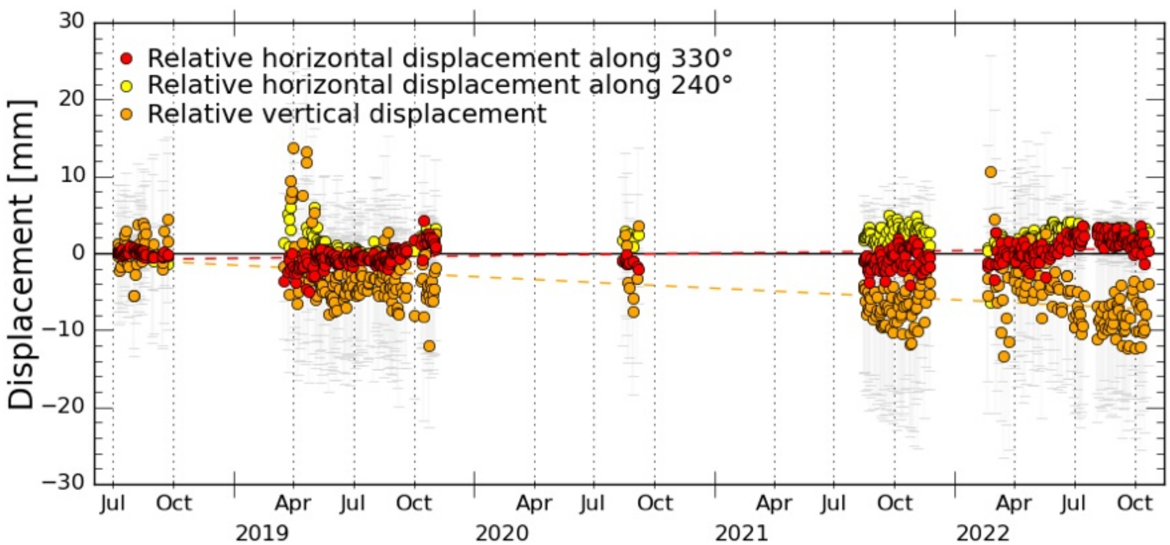

Figure 11. Corrected displacement of the CGNSS station north of the fracture (SVIN) since July 2018. Error bars are indicated by grey horizontal lines. Colored dashed lines are linear interpolations of the data points of the same color. – *Leiðrétt færsla CGNSS stöðvarinnar norðan við sprunguna (SVIN) frá júlí 2018. Óvissa eru sýndar með gráum láréttum línum.*

ture logger "FRT" was lowered 8 m into a bedrock fracture at the highest point of the main fracture (locations shown in Figure 3c). Throughout the two-year period the temperatures measured by "FRT" never went below 0°C. After a short decrease in temperature in fall the temperature variations stay within 1 degree between October and June. For the presented time series all RST loggers record mean annual temperatures above 0°C (Table 2). The back-calculated temperature data for RST 1–4 locations is presented in Figure 12b. According to the calculations, the only station which experienced sub-0°C temperatures since the end of the LIA is RST1 which lies about 200 m higher than the highest mapped fracture. Moreover, the calculated temperature development shows that the two stations which lie within the area bound by the main fracture (RST3 and 4) have not experienced conditions favorable for permafrost formation since 1898.

Table 2. Mean annual rock surface temperature data over two years. – *Meðaltal árlegs berghitastigs á tveggja ára tímabili.*

Name	Aspect azimuth [°]	Elevation [m a.s.l.]	2020–2021 [°C]	2021–2022 [°C]	2-year mean [°C]
RST 1	344	1093	0.65	0.83	0.74
RST 2	2	926	1.92	2.1	2.01
RST 3	342	846	2.24	2.57	2.4
RST 4	355	803	2.15	2.65	2.4
FRT	–	840	1.1	1.14	1.12

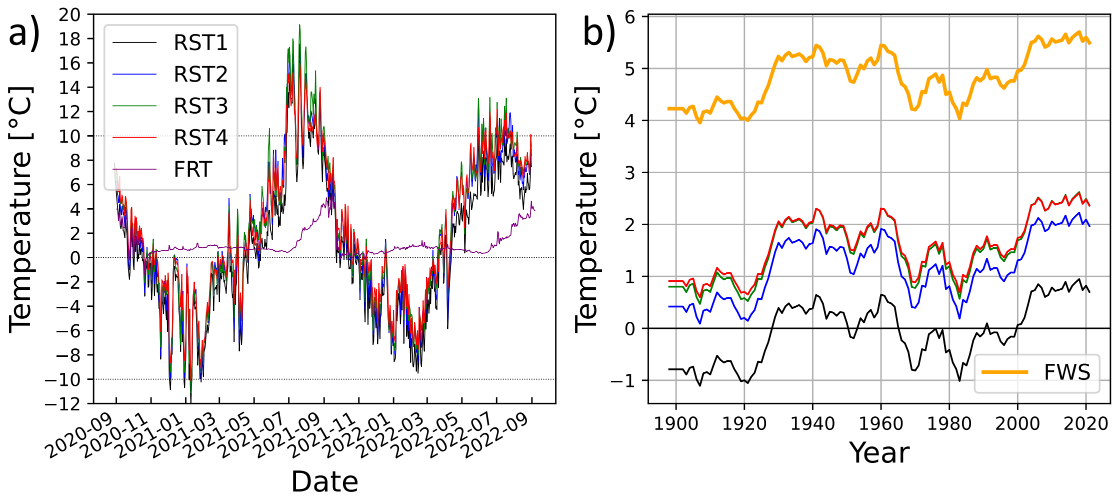

Figure 12. Panel a) shows two years of recorded temperature data at locations marked in Figure 2. b) The orange graph shows the rolling mean over mean annual air temperatures at Fagurhólsmýri weather station (FWS) and the back-calculated RST graphs are illustrated in the respective colors as the RST measurements in a) on which they are based. – *a) Niðurstöður tveggja ára hitamælinga. Hitamælarnir RST 1–4 voru boraðir inn í bergið og FRT er sigið niður ∼8 m í sprungu, sjá 2. mynd. b) Appelsínugula línan sýnir hlaupandi meðaltal meðalhitastigs samkvæmt veðurstöðinni á Fagurhólsmýri (FWS).*

DISCUSSION

Morphological evidence of past landslide activity

A cluster of paraglacial landslides have been observed in the mountains by Svínafellsjökull. Evidence of past landslide activity is present in eastern Svínafellsfjall, where it forms a hanging, half eroded U-shaped valley with the slope of Skarðatindur (Figure 5e). U-shaped valleys are typically formed through glacial erosion (Benn and Evans, 2010). The last time this area was glaciated was likely at the end of the LGM (Guðmundsson, 1998). However, further east, where a potential catchment for the glacier would have been, the plateau abruptly ends in a steeply eroded slope of volcanic layers (Figure 5b) and Dyrhamarsjökull in the valley below (Figure 4). Further evidence of a bigger original drainage catchment is the extent of Svarthamragil canyon that lies at the bottom of this half-U-shaped valley (Figure 5e). The linear nature of Svarthamragil canyon indicates that there might be, to some extent, a structural control to the canyon. The up to 50 m deep canyon is partly dry, hosts only a creek and has a small catchment that is unlikely to provide enough energy to form this feature. The water catchment, too, ends at the steeply eroded slope mentioned earlier (Figure 5b). These observations indicate that a large part of the mountain that hosted a glacier, and a post-glacial water drainage, forming Svarthamragil canyon, has been removed, potentially during the Holocene. Similar hanging valleys, not occupied by glaciers, have been observed at Aconcagua volcano in the Argentine Andes where they were related to large mountain slope failures (Fauqué *et al.*, 2009; Hermanns *et al.*, 2015).

Two bowl-shaped features with scarp-like headwalls were described on Svarthamrar (Figures 4 and 5a,f). Those formations are unlike fluvially eroded valleys as there is no dominating water channel on the slope. A glacial origin is unlikely since no glacial landforms or sediments were observed on the slope. The geometry of these features indicates that they could have been formed by the removal of material through compound landslides with a rotational component in the upper part and translational sliding in the lower part.

The frontal moraines of Svínafellsjökull have been described to be higher above the surrounding terrain and contain a higher fraction of angular shaped clasts than moraines at neighboring outlet glaciers (Thompson, 1988; Everest *et al.*, 2017; Lee *et al.*, 2018) which suggests more supraglacially derived debris at Svínafellsjökull. Debris of supraglacial landslides can either reach the glacier margin by runout or by being transported there by the glacier flow (Schleier *et al.*, 2015) and they are often difficult to distinguish from classical moraine sediments.

Considering recent landslide activity and the described geomorphology it seems likely that the catchment of Svínafellsjökull has experienced repeated rock slope failures during the Holocene. Especially on Svarthamrar, the absence of a catchment for a valley eroding glacier and the two bowl-shaped landslide scars indicate significant amounts of removed material that should have been transported into the outwash plain or into the moraine depending on the extent of the glacier at the time of the failure.

Paraglacial slopes that lie at the inner bend of a glacier turn (top-down convex mountain outline) commonly seem to be affected by mass movements over large parts of the slope. This has been observed at Steinsholtsjökull (Kjartansson, 1967), Tungnakvíslarjökull (Lacroix *et al.*, 2022), Tindfjallajökull (Arnar, 2021), and Svarthamrar (Figures 4 and 2) and is likely due to more aspects being exposed to gravitational forces.

Fracture features and their implications

The Svarthamrar slope instability is outlined by an almost 2 km long line of sinkholes and bedrock fractures separating the northernmost part of the mountain. Along this line we can infer a connected bedrock fracture system that defines an area of 0.9 km^2 between the fracture and the glacier (Figure 4). Further downslope (north) several aligned sinkholes are connected by inferred fractures. Single sinkholes across the slope suggest that a more extensive bedrock fracture network has formed underneath the soil cover north of the main fracture but is likely not developed enough to form more extensive sinkholes. The documented fractures are interpreted as tension cracks which open due to tensile stress within the bedrock (Wyllie, 2017). The absence of diffuse structures such as double ridges and counter scarps indicates that most of the displacement has been taking place along these tension cracks, largely below the soil cover. It further suggests that the limiting structures along the failure surface are not fully developed yet. No observed vertical offset at the tension cracks suggests a rather horizontal translational movement of the slope towards the north, orthogonal to the fractures. The fact that the inferred fracture network runs through different lithologies across 450 m of elevation change on the slope suggests that the main fracture penetrates deep into the bedrock. This indicates that the incipient failure surface (British Standards Institution, 2015) penetrates to considerable depth and that the shallower stratigraphic northwest dipping and daylighting discontinuities described in Helgason and Duncan (2013) are unlikely to act as a sliding surface in this case. The tension cracks indicate increased tensile stresses throughout the slope which can be a sign of a range of deformation processes. They are most likely created by internal toppling motion within the rock mass and/or translatory motion on a deep failure plane. Toppling motion in bedrock slopes can occur during the initial stages of a large rotational slope failure (Wyllie, 2017). Therefore, possible deformation kinematics of this slope are a translatory slide with a deep tension crack at the back, a rotational slide, or a compound slide combining both, translatory and rotational deformation. Because of the unknown geometry of the incipient failure surface, volume estimates are difficult. Based on the surface area of deformation (ca. 0.9 km^2) and described evidence of a likely deep-seated instability a volume range of 50–150x10^6 m^3 is realistic. 200–300 m tall, near-vertical headscarps have been documented at paraglacial rock slope failures in Iceland (Kjartansson, 1967; Sæmundsson *et al.*, 2011; Lacroix *et al.*, 2022) with similar volcanic stratigraphy (Loughlin, 2002; Torfason and Jónsson, 2005; Helgason and Duncan, 2013) suggesting that the Svarthamrar slope instability may form a similarly tall headscarp during a future failure.

Partial slope failures are common in large unstable rock slopes (Agliardi *et al.*, 2012; Klimeš *et al.*, 2021; Kristensen *et al.*, 2021). The headscarp of the 2013 debris avalanche is located in the linear extension of the main fracture (Figure 4). This suggests that the same structural discontinuity in the bedrock might have been partly responsible for the failure of the mostly sediment derived 2013 debris avalanche. If true, then the 2013 debris avalanche can be considered a partial failure of the Svarthamrar slope instability.

The main bedrock fracture on Svarthamrar has a certain similarity with the so called "narrow bottomless crack" that was described on Mt. Innstihaus some 7–8 years before the catastrophic rockslide onto Steinsholtsjökull glacier in 1967 which had developed into a "one foot wide" fracture by autumn 1966 (Kjartansson, 1967). The original fracture was only 160 m long whereas the headscarp after failure was 900 m long. At the source area of the rock avalanche onto Morsárjökull glacier in 2007 no bedrock fractures were documented in 2003 imagery (Decaulne *et al.*, 2010; Sæmundsson *et al.*, 2011). These examples highlight that large catastrophic rock slope failures in these volcanic rocks can occur with little, short-term, and small-scale pre-failure slope deformation concentrated on horizontally opening fractures and without the failure surface fully developed. This is different to what is expected using the Norwegian hazard classification system (Hermanns *et al.*, 2013), which suggests that ideally all limiting structures are fully developed prior to a catastrophic failure.

Timing of the slope destabilization

A single sinkhole already formed between 1968 and 1980 indicates the existence of a bedrock fracture separating a part of the cliff Rák (Figure 4). This feature lies north of the described main fracture and shows that an isolated part of the slope has been developing a tension crack 2–4 decades before the main part of the Svarthamrar slope instability was initiated. However, the main phase of deformation was initiated after 2003 (Figure 9).

Our image analysis indicates that the surface expression of the main fracture started forming sometime between 2003 and 2007 (Figures 7 and 9). A time lag between bedrock fracture opening and formation of sinkholes can be expected where soil thickness, and vegetation stabilizes the material above the bedrock fracture. This is likely to be dependent on fracture width and water input into the soil (Tharp, 2003). Given that the fractures have been observed to continue under completely intact soil cover (Figures 3b,d) shows that the fractures first form underneath the sediment which then gradually collapses into the underlying, expanding void. The sinkholes across the slope became more pronounced throughout the years 2009 to 2020. The presented InSAR data (Figure 10) shows that the slope was deforming between 2015 to 2017 and no noticeable activity has occurred since then. Before 2015 we have no imagery to determine the deformation rate with InSAR. The two differently moving segments may be a result of a change in the geometry of the sliding surface and/or might indicate rotational movement. However, since north-motion is not resolved in the InSAR analysis only the east-west and up-down components are visible of what is likely a general movement to the north based on the slope morphology and tension crack orientation. Repeated tape measurements show a halt of deformation at the uppermost fracture in 2018 (Table 1) and CGNSS and extensometer measurements confirm no significant movement after the summer of 2018. The onset of the Svarthamrar slope instability occurred between 2003 and 2007. The phase of deformation along the main fracture lasted until 2017 which means a deformation time of maximum 10–14 years. With the main fracture being up to 40 cm wide, a maximum deformation rate of 2.8–4 cm/yr orthogonal to the fractures can be derived, given the deformation was a continuous process.

The role of glacial changes

The fastest documented glacier thinning since 1890 occurred between 1994 and 2011. Almost 50 m of ice thickness was lost which led to a significant reduction of loading on the subglacial slope (Figure 9). This likely increased tensile stresses throughout the slope, forming vertical tension cracks and sinkholes as the slope adjusted to the new boundary conditions. The debris avalanche deposits from 2013 reset the glacier load at the bottom of the slope to approximately the year 2007 (Figure 9b) and protect the underlying glacier from ablation. The slope deformation stopped in 2017 suggesting that there was a time lag between a halt of glacial thinning and slope adjustment. We hypothesize that the described slope deformation is somewhat controlled by glacier surface elevation and changes of glacier load on the subglacial slope.

If the incipient failure surface daylights above the current glacier surface it is likely that the slope will not be affected by future glacial retreat. Based on our observations and similar slope failures elsewhere in Iceland it is, however, more likely that the incipient failure surface daylights below the glacier surface. In this case further slope deformation and potential failure is probable with future glacial thinning. Glacial thinning in front of the Svarthamrar slope instability is currently only partly mass balance driven since it has been affected by the insulating effect of the debris avalanche deposits from the 2013 (Ben-Yehoshua *et al.*, 2022). With the current ice-flow velocity of about 120 m/yr, the 2013 debris avalanche deposits will have completely passed the area in front of the Svarthamrar slope instability in ca. 2031. This process will gradually re-expose the glacier surface in front of the Svarthamrar slope instability to ablation and reduce the excess load of the debris from the subglacial slope, leading to simultaneously increasing tensile stresses within the slope. These forces are likely to reactivate the progressive rock damage and further development of limiting structures which may result in partial or complete failure of the slope (Klimeš *et al.*, 2021). While glacier debuttressing has been identified as a destabilizing factor for alpine rock slopes, more structurally damaged slopes with higher strain rates can lead to ductile or brittle glacier deformation, further increasing the tensile stresses in the slope (McColl and Davies, 2013). This is a likely future scenario for the Svarthamrar slope instability.

Mass balance modelling of the Vatnajökull Ice Cap based on different climate scenarios predict a slow but continuous mass-loss until the mid-21st century and then accelerated ice mass loss (Schmidt *et al.*, 2019; Noël *et al.*, 2022). The rate of ice mass loss is strongly dependent on different greenhouse gas scenarios but in either scenario there is a high confidence that the glacier will lose more ice in the coming decades due to ongoing climate change (Schmidt *et al.*, 2019; Noël *et al.*, 2022). A further retreat of Svínafellsjökull would increase the size of the proglacial lakes and therefore increase the chance of a potential catastrophic failure of the Svarthamrar slope instability causing a displacement wave (Kjartansson, 1967; Higman *et al.*, 2018; Byers *et al.*, 2019; Dai *et al.*, 2020; Klimeš *et al.*, 2021; Geertsema *et al.*, 2022).

This deglaciation trend over the next decades and centuries is not only true for Svínafellsjökull but most glaciers worldwide which will lead to further debuttressing and unloading of mountain slopes and an increased potential for new and large slope instabilities.

The role of permafrost

Since the study area lies in glaciated alpine terrain, degradation of mountain permafrost was considered as a potential destabilizing factor (Huggel *et al.*, 2012; Etzelmüller *et al.*, 2022; Penna *et al.*, 2022). According to permafrost models the area lies just at the lower boundary of sporadic mountain permafrost (Obu *et al.*, 2019) or completely outside the calculated permafrost zones (Czekirda *et al.*, 2019). Presented temperature measurements on snow-free, near-vertical and north-facing slopes in the study area show that recent annual RST are clearly above 0°C up to an elevation of 1093 m a.s.l. (Table 2). The air temperature measured at a depth of 8 m at the highest point of the main fracture at 840 m elevation shows that snow cover insulates the air in the fracture for about

8 months per year. During this timeframe the fracture temperature stays above 0°C (Figure 12). Therefore we can exclude freezing of fractures due to cool air sinking into the crack (Blikra and Christiansen, 2014). The combination of unfavorable conditions for permafrost formation in both, fractures and in steep, north-facing rock walls suggest that the study area currently does not have the right conditions to form or preserve permafrost since a temperature of <0°C is required (Dobinski, 2011).

To investigate whether some mountain permafrost could be preserved from the LIA the temperature trends for RST1-4 were back-calculated using a linear regression model (Figure 12b). According to these results the highest RST logger location, RST1 at 1093 m elevation went through phases in the last 130 years when annual temperatures were below 0°C and thus favorable for permafrost formation. This, however, is the only measurement point where the back-calculated average annual temperature temporarily reached below freezing temperature in 131 years. The annual temperatures stayed well above 0°C throughout the entire timespan at RST 2, 3 and 4 (RST 3 and 4 lie within the Svarthamrar slope instability, Table 2). This indicates unfavorable conditions for permafrost formation on Svarthamrar throughout the 20th and early 21st century. Since the loggers were mounted on north-facing slopes the temperatures at these locations can be expected to be lower than other aspects (Hasler *et al.*, 2011). Our results are therefore in accordance with predictions made by Etzelmüller *et al.* (2007) and Czekirda *et al.* (2019) that permafrost is likely absent at present day on Svarthamrar.

In the coming decades, climate change driven glacier retreat, temperature rise, permafrost degradation (Chiarle *et al.*, 2021) and more precipitation (Björnsson *et al.*, 2018) are likely to further destabilize rock-slopes in Iceland and similar environments worldwide.

CONCLUSIONS

Our observations of present-day morphology indicate that Svínafellsfjall has likely been undergoing significant modification through mass movements during the Holocene. The current cluster of slope instabilities in the valley supports the theory that landslide activity has been common in the glacier catchment.

A 2 km long fracture system delimits the Svarthamrar slope instability, in northeastern Svínafellsfjall. The first signs of bedrock fracturing on the slope have been observed already in 1980 imagery. However, the main Svarthamrar slope instability, defined by an area of 0.9 km^2 between the main fracture and the glacier was initiated between 2003 and 2007 and continued to evolve until 2017. Based on the characteristics of the deformation structures we suggest a deep-seated incipient failure surface which may develop into a rotational or composite rockslide with a minimum volume range of 50–150$\times$10^6 m^3.

The increased tensile stresses in the mountain slope, necessary to form the extensive network of tension cracks, are likely a result of decreased supportive forces due to rapid glacial thinning between 1994 and 2011. The lack of movement since 2017 suggests that the mountain slope has reached a temporary force equilibrium with the debris covered glacier. As the 2013 debris avalanche deposits are transported down-glacier the tensile stresses in the slope are likely to increase again, re-activating the deformation.

Therefore, it is crucial to continue the monitoring of the Svarthamrar slope instability to be able to provide an early warning in case of a renewed onset and potential acceleration of the slope deformation. A future study should include a detailed structural geological analysis and slope stability modelling based on different glacier retreat scenarios. This is important to understand the slope kinematics and to better assess the hazard the slope poses to humans and infrastructure. The described Svarthamrar slope instability clearly demonstrates the potential scale of consequences of the rapid climatic changes which have been taking place in the glacial and alpine environments over the last century. These climatic changes are predicted to continue globally, resulting in more frequent paraglacial slope instabilities.

Acknowledgements

We want to thank the Icelandic Research Fund (grant number: 207136-053) and the Energy Research Fund from the National Power Company of Iceland (grant number: NÝR-06–2020, NÝR-09–2021, NÝR-10—2022) for financing this study. Dr. Susan Conway and Dr. Kristian Svennevig provided the study with invaluable feedback during the review process for which we are very grateful. The study was further supported through the great commitment and enthusiasm of field assistants Sydney Gunnarson, Dr. Robert Askew, Victor Pajuelo Madrigal, Árni Stefán Haldorsen and Daniel Saulite during long days in difficult terrain. Additionally, we would like to thank Íris Ragnarsdóttir Pedersen, Árni Stefán Haldorsen, Hafdís Sigrún Roysdóttir, Svanhvít Helga Jóhannesdóttir and Daniel Saulite for providing the first author with accommodation and wonderful company during his stays in Svínafell. We thank Dr. Florence Magnin for her feedback regarding temperature regression methods, and Dr. Jóhann Helgason for sharing his in-depth knowledge of the geology in the study area. Svarmi ehf. assisted this study with crucial equipment for UAV surveys and temperature measurements as well as access to software for data processing. Pix4D supported this study with necessary photogrammetric software for which we are very grateful. Furthermore, we acknowledge Loftmyndir ehf. who provided the elevation model from 2003.

ÁGRIP

Eftir að litlu ísöld lauk í lok síðustu aldar hafa íslenskir jöklar hopað verulega. Í kjölfar þynningar og hopun jökla standa oft eftir brattar og óstöðugar hlíðar, sem með tímanum geta aflagast og jafnvel hlaupið fram í hamfaraatburðum. Hér er lýst hreyfingum á nokkrum bergmössum umhverfis Svínafellsjökuls á suðausturhorni landsins. Stærstar þessar hreyfinga eru í norður hlíð Svínafellsfjalls þar sem um það bil 2 km langt sprungukerfi hefur verið kortlagt á yfirborði. Allt að um 1 km^2 svæði er óstöðugt neðan sprungunnar og er áætlað að rúmmálið sé á milli 50 og 150×10^6 m^3. Á yfirborði í þessari óstöðugu fjallshlíð hafa um 200 ílöng jarðföll verið kortlögð, þar sem efni á yfirborði hafa fallið ofan í undirliggjandi bergsprungur. Athuganir með ýmsum fjarkönnunargögnum, frásögnum sjónarvotta og kortlagningar á staðnum gefa til kynna að sprungukerfið hafi myndast á tímabilinu frá 2003 til 2007. Þetta á sér stað á sama tíma og þynning jökulsins var hvað hröðust á síðastliðnum 131 árum. Frá árinu 2011 hefur jökullinn ekki þynnst mikið, og má að líkindum leita hluta skýringa á því að árið 2013 féll skriða á jökulinn og hefur skriðuefnið einangrað jökulinn og hægt á bráðnun hans. Mælingar sýndu hreyfingar á hlíðinni fram til ársins 2017. Á því ári var komið fyrir mælitækjum á sprunguna en síðan þá hefur lítil sem engin hreyfing mælst. Stórt brotsár í hlíðum dalsins ofan jökulsins og efnismiklir endagarðar með stórum bergbrotum fyrir framan jökulinn gefa til kynna að berghlaup hafi áður fallið á jökulinn. Nýlegar hitastigsmælingar í berginu umhverfis jökulinn, ásamt eldri veðurfarsgögnum benda ekki til þessa að þiðnun sífrera hafi orsakað þessar hreyfingar. Niðurstöður athuganna sem kynntar eru hér benda til þess að hop og þynning jökla vegna loftslagsbreytinga hafi og muni hafa frekari áhrif á stöðugleika brattra fjallshlíða í nágrenni íslenskra jökla.

REFERENCES

Aðalgeirsdóttir, G., E. Magnússon, F. Pálsson, T. Thorsteinsson, J. M. C. Belart, T. Jóhannesson, H. Hannesdóttir, O. Sigurðsson, A. Gunnarsson, B. Einarsson, E. Berthier, L. S. Schmidt, H. H. Haraldsson and H. Björnsson 2020. Glacier Changes in Iceland from ∼1890 to 2019. *Front. Earth Sci.* 8, 1–15. http://doi.org/10.3389/feart.2020.523646

Agliardi, F., G. B. Crosta and P. Frattini 2012. Slow rock slope deformation. In: *Landslides: types, mechanisms and modelling.* Cambridge University Press, 207–221.

Altamimi, Z., L. Métivier and X. Collilieux 2012. ITRF2008 plate motion model. *J. Geoph. Res.: Solid Earth* 117, 1–14. https://doi.org/10.1029/2011JB008930

Arnar, E. 2021. *Geomorphological mapping of a paraglacial slope instability at the southeastern Tindfjallajökull glacier, Iceland.* B.Sc. Thesis, U. Iceland, 51 pp. http://hdl.handle.net/1946/39947

Ballantyne, C. K. 2002. Paraglacial Geomorphology. *Encyclopedia of Quaternary Science: 2nd ed.* 21, 553–565. https://doi.org/10.1016/B978-0-444-53643-3.00089-3

Ballantyne, C. K., G. F. Sandeman, J. O. Stone and P. Wilson 2014. Rock-slope failure following Late Pleistocene deglaciation on tectonically stable mountainous terrain. *Quat. Sci. Rev.* 86, 144–157. https://doi.org/10.1016/j.quascirev.2013.12.021

Belart, J. M. C., E. Magnússon, E. Berthier, Á. Gunnlaugsson, F. Pálsson, G. Aðalgeirsdóttir, T. Jóhannesson, T. Thorsteinsson and H. Björnsson 2020. Mass Balance of 14 Icelandic Glaciers, 1945–2017: Spatial variations and links with climate. *Front. Earth Science* 8, 163. https://doi.org/10.3389/feart.2020.00163

Ben-Yehoshua, D. 2016. Drone imaging of a potentially hazardous slope on Svínafellsheiði, SE-Iceland. A new approach to mass movement prediction. *Rannís Student Innovation Fund - Final Report,* 27 pp.

Ben-Yehoshua, D. and S. Gunnarson 2018. *UAV imaging of the lower fracture at Svínafellsheiði South East Iceland, September 2018, Description of the Project and Dataset.* Svarmi ehf. Project report for Icelandic Meteorological Office, 8 pp.

Ben-Yehoshua, D., Þ. Sæmundsson, J. K. Helgason, J. M. C. Belart, J. V. Sigurðsson and S. Erlingsson 2022. Paraglacial exposure and collapse of glacial sediment: The 2013 landslide onto Svínafellsjökull, southeast Iceland. *Earth Surface Processes and Landforms* 47(10), 2612–2627.
https://doi.org/10.1002/esp.5398

Benn, D. I. and D. J. A. Evans 2010. *Glaciers and Glaciation, 2nd ed.* 303–308. Routledge, London.

Bessette-Kirton, E. K. and J. A. Coe 2020. A 36-year record of rock avalanches in the Saint Elias mountains of Alaska, with implications for future hazards. *Front. Earth Science* 8, 1–23.
https://doi.org/10.3389/feart.2020.00293

Björnsson, H., B. D. Sigurðsson, B. Davíðsdóttir, J. Ólafsson, Ó. S. Ástþórsssson, S. Ólafsdóttir, T. Baldursson and T. Jónsson 2018. *Climate Change and its effects in Iceland.* Report of the Scientific Committee on Climate Change 2018 (in Icelandic). 237 pp.

Blikra, L. H. and H. H. Christiansen 2014. A field-based model of permafrost-controlled rockslide deformation in northern Norway. *Geomorphology* 208, 34–49.

British Standards Institution BS 5930: 2015, *Code of Practice for Ground Investigations*, 4th ed., 143–150, BSI Standards Limited 2015, London.

Böðvarsson, B. I. 2004. *Jarðefni, þjöppun og samanburður aðferða við þjöppumælingar.* Technical University of Iceland, 163 pp. https://www.vegagerdin.is/Vefur2.nsf

Böhme, M., T. Oppikofer, O. Longva, M. Jaboyedoff, R. L. Hermanns and M. H. Derron 2015. Analyses of past and present rock slope instabilities in a fjord valley: Implications for hazard estimations. *Geomorphology* 248, 464–474.
https://doi.org/10.1016/j.geomorph.2015.06.045

Chiarle, M., M. Geertsema, G. Mortara and J. J. Clague 2021. Relations between climate change and mass movement: Perspectives from the Canadian Cordillera and the European Alps. *Global and Planetary Change* 202, 103499.
https://doi.org/10.1016/j.gloplacha.2021.103499

Coquin, J., D. Mercier, O. Bourgeois, E. Cossart and A. Decaulne 2015. Gravitational spreading of mountain ridges coeval with Late Weichselian deglaciation: Impact on glacial landscapes in Tröllaskagi, northern Iceland. *Quat. Sci. Rev.* 107, 197–213.
https://doi.org/10.1016/j.quascirev.2014.10.023

Cossart, E., D. Mercier A. Decaulne and T. Feuillet 2013. An overview of the consequences of paraglacial landsliding on deglaciated mountain slopes: Typology, timing and contribution to cascading fluxes. *Quaternaire* 24, 13–24. https://doi.org/10.4000/quaternaire.6444

Cruden, D. M. and X. Q. Hu 1993. Exhaustion and steady state models for predicting landslide hazard in the Canadian Rockies. *Geomorphology* 8, 279–285.

Cuffey, K. M. and W. S. B. Paterson 2010. *The Physics of Glaciers*, 4th ed., 11–28.

Czekirda, J., S. Westermann, B. Etzelmüller and T. Jóhannesson 2019. Transient modelling of permafrost distribution in Iceland. *Front. Earth Sci.* 7, 23 pp.
https://doi.org/10.3389/feart.2019.00130

Dabiri, Z., D. Hölbling, L. Abad, J. K. Helgason, Þ. Saemundsson and D. Tiede 2020. Assessment of landslide-induced geomorphological changes in Hítardalur Valley, Iceland, using Sentinel-1 and Sentinel-2 data. *Applied Sciences* 10, 12–14.
https://doi.org/10.3390/app10175848

Dai, C. *et al.* 2020. Detection and assessment of a large and potentially tsunamigenic periglacial landslide in Barry Arm, Alaska. *Geophys. Res. Lett.* 47.
https://doi.org/10.1029/2020GL089800

Decaulne, A., E. Cossart, D. Mercier, T. Feuillet, J. Coquin and H. P. Jónsson 2016. An early Holocene age for the Vatn landslide (Skagafjörður, central northern Iceland): Insights into the role of postglacial landsliding on slope development. *Holocene* 26, 1304–1318.
https://doi.org/10.1177/0959683616638432

Decaulne, A., Þ. Sæmundsson, H. G. Pétursson, I. A. Jónsson and I. A. Sigurðsson 2010. A large rock avalanche onto Morsárjökull glacier, south-east Iceland. Its implications for ice-surface evolution and glacier dynamics. *Iceland in the Central Northern Atlantic: hotspot, sea currents and climate change.* Plouzane, France, 6–8. http://hal.univ-brest.fr/hal-00482107

Deline, P., S. Gruber, F. Amann, X. Bodin, R. Delaloye, J. Failletaz, L. Fischer, M. Geertsema, M. Giardino, A. Hasler and M. Kirkbride 2021. Ice loss from glaciers and permafrost and related slope instability in high-mountain regions. In: *Snow and ice-related hazards, risks, and disasters*, Elsevier.501–540.

Deline, P., K. Hewitt, N. Reznichenko and D. Shugar 2014. Rock Avalanches onto Glaciers. In: *Landslide Hazards, Risks, and Disasters* 263–319.

Dobinski, W. 2011. Permafrost. *Earth Sci. Rev.* 108, 158–169. https://doi.org/10.1016/j.earscirev.2011.06.007

Drouin, V. and F. Sigmundsson 2019. Countrywide observations of plate spreading and glacial isostatic adjustment in Iceland inferred by Sentinel-1 radar interferometry, 2015–2018. *Geophys. Res. Lett.* 46, 8046–8055. https://doi.org/10.1029/2019GL082629

Dufresne, A. *et al.* 2018. Sedimentology and geomorphology of a large tsunamigenic landslide, Taan Fiord, Alaska. *Sedim. Geology* 364, 302–318. https://doi.org/10.1016/j.sedgeo.2017.10.004

Dufresne, A., G. J. Wolken, C. Hibert, E. K. Bessette-Kirton, J. A. Coe, M. Geertsema and G. Ekström 2019. The 2016 Lamplugh rock avalanche, Alaska: deposit structures and emplacement dynamics. *Landslides* 16, 2301–2319. https://doi.org/10.1007/s10346-019-01225-4

Eberhardt, E., D. Stead and J. S. Coggan 2004. Numerical analysis of initiation and progressive failure in natural rock slopes-the 1991 Randa rockslide. *Int. J. Rock Mechanics and Mining Sci.* 41, 69–87. https://doi.org/10.1016/S1365-1609(03)00076-5

Einarsson, P. 2019. Historical accounts of pre-eruption seismicity of Katla, Hekla, Öræfajökull and other volcanoes in Iceland. *Jökull* 69, 35–52. https://doi.org/10.33799/jokull2019.69.035

Etzelmüller, B. *et al.* 2022. Permafrost in monitored unstable rock slopes in Norway – new insights from temperature and surface velocity measurements, geophysical surveying, and ground temperature modelling. *Earth Surface Dynamics* 10, 97–129. https://doi.org/10.5194/esurf-10-97-2022

Etzelmüller, B., H. Farbrot, Á. Guðmundsson, O. Humlum, O. E. Tveito and H. Björnsson 2007. The regional distribution of mountain permafrost in Iceland. *Permafrost and Periglacial Proc.* 18, 185–199. https://doi.org/10.1002/ppp.583

Evans, S. G., N. F. Bishop, l. Fidel Smoll, P. Valderrama Murillo, K. B. Delaney and A. Oliver-Smith 2009. A re-examination of the mechanism and human impact of catastrophic mass flows originating on Nevado Huascarán, Cordillera Blanca, Peru in 1962 and 1970. *Engineering Geology* 108, 96–118. https://doi.org/10.1016/j.enggeo.2009.06.020

Evans, S. G. and J. J. Clague 1988. Catastrophic rock avalanches in glacial environments. *Proceedings of 5th International Symposium on Landslides* 2, 1153–1158.

Evans, S. G. and J. J. Clague 1994. Recent climatic change and catastrophic geomorphic processes in mountain environments. *Geomorphology and natural hazards* 10, 107–128. https://doi.org/10.1016/b978-0-444-82012-9.50012-8

Everest, J., T. Bradwell, L. Jones and L. Hughes 2017. The geomorphology of Svínafellsjökull and Virkisjökull-Falljökull glacier forelands, Southeast Iceland. *J. Maps* 13, 936–945. https://doi.org/10.1080/17445647.2017.1407272

Fan, X. *et al.* 2020. The formation and impact of landslide dams – State of the art. *Earth Sci. Rev.* 203, 103116. https://doi.org/10.1016/j.earscirev.2020.103116

Fauqué, L., R. Hermanns, K. Hewitt, M. Rosas, C. Wilson, V. Baumann, S. Lagorio and I. Di Tommaso 2009. Mega-deslizamientos de la pared sur del cerro aconcagua y su relación con depósitos asignados a la glaciación pleistocena. *Revista de la Asociacion Geologica Argentina* 65, 691–712.

Geertsema, M. *et al.* 2022. The 28 November 2020 landslide, tsunami, and outburst flood – a hazard cascade associated with rapid deglaciation at Elliot Creek, British Columbia, Canada. *Geophys. Res. Lett.* 49. https://doi.org/10.1029/2021GL096716

Geirsson, H. *et al.* 2018. *Reawakening of the Öræfajökull volcano in Iceland: deformation signals of stress triggers and intrusive activity.* EGU General Assembly Conference Abstract 15438.

Grämiger, L. M., J. R. Moore, V. S. Gischig, S. Ivy-Ochs and S. Loew 2017. Beyond debuttressing: Mechanics of paraglacial rock slope damage during repeat glacial cycles. *J. Geophys. Res.: Earth Surface* 122, 1004–1036. https://doi.org/10.1002/2016JF003967

Grämiger, L. M., J. R. Moore, V. S. Gischig and S. Loew 2018. Thermomechanical stresses drive damage of alpine valley rock walls during repeat glacial cycles. *J. Geophys. Res.: Earth Surface* 123, 2620–2646. https://doi.org/10.1029/2018JF004626

Gruber, S. and W. Haeberli 2008. Mountain permafrost. *Soil Biology* 16, 33–44. https://doi.org/10.1007/978-3-540-69371-0_3

Guðmundsson, H.J. 1998. *Holocene glacier fluctuations and tephrochronology of the Öræfi district, Iceland.* PhD Thesis, University of Edinburgh, 284 pp.

Gudmundsson, M.T., G. Larsen, Á. Höskuldsson, Á.G. Gylfason 2008. Volcanic hazards in Iceland. *Jökull* 58, 251–268. https://doi.org/10.33799/jokull2008.58.251

Guðmundsson, S., H. Björnsson, F. Pálsson, E. Magnússon, T. Sæmundsson and T. Jóhannesson 2019. Terminus lakes on the south side of Vatnajökull ice cap, SE-Iceland. *Jökull* 69, 1–34. https://doi.org/10.33799/jokull2019.69.001

Hannesdóttir, H., H. Björnsson, F. Pálsson, G. Aðalgeirsdóttir and S. Guðmundsson 2015. Changes in the southeast Vatnajökull ice cap, Iceland, between ∼1890 and 2010. *Cryosphere* 9, 565–585. https://doi.org/10.5194/tc-9-565-2015

Hartmeyer, I., R. Delleske, M. Keuschnig, M. Krautblatter, A. Lang, J. Christoph Otto and L. Schrott 2020. Current glacier recession causes significant rockfall increase: The immediate paraglacial response of deglaciating cirque walls. *Earth Surface Dynamics* 8, 729–751. https://doi.org/10.5194/esurf-8-729-2020

Hasler, A., S. Gruber and W. Haeberli 2011. Temperature variability and thermal offset in steep alpine rock and ice faces. *Cryosphere* 5, 977–988. https://doi.org/10.5194/tc-5-977-2011

Helgason, J. and R.A. Duncan 2001. Glacial-interglacial history of the Skaftafell region, southeast Iceland, 0–5 Ma. *Geology* 29, 179–182.

Helgason, J. and R.A. Duncan 2013. Stratigraphy, ^{40}Ar–^{39}Ar dating and erosional history of Svínafell, SE-Iceland. *Jökull* 63, 33–54. https://doi.org/10.33799/jokull2013.63.033

Helgason, J.K., C. Morino, S.J. Conway, Þ. Saemundsson and M.R. Balme 2018. *On the dynamics of permafrost-induced landslides in Iceland.* EUCOP5, conference paper, Chamonix, France 23.

Hermanns, R.L., T. Oppikofer, E. Anda, L.H. Blikra, M. Bohme *et al.* 2013. Hazard and risk classification for large unstable rock slopes in Norway. *Italian J. Eng. Geology and Environment*, 245–254. https://doi.org/10.4408/IJEGE.2013-06.B-22

Hermanns, R.L., L. Fauqué and C.G.J. Wilson 2015. ^{36}Cl terrestrial cosmogenic nuclide dating suggests Late Pleistocene to Early Holocene mass movements on the south face of Aconcagua mountain and in the Las Cuevas-Horcones valleys, Central Andes, Argentina. *Geol. Soc. Spec. Pub.* 399, 345–368. https://doi.org/10.1144/SP399.19

Hermanns, R.L. and O. Longva 2013. Rapid rock-slope failures. *Landslides, Types, Mechanisms and Modeling* Ch. 6, 59–70. https://doi.org/10.1017/cbo9780511740367.007

Hermanns, R.L., S. Niedermann, G.A. Villanueva and A. Schellenberger 2006. Rock avalanching in the NW Argentine Andes as a result of complex interactions of lithologic, structural and topographic boundary conditions, climate change and active tectonics. In: *Landslides from massive rock slope failure: Proc. of the NATO advanced research workshop on massive rock slope failure - new models for hazard assessment*. Springer. 497–520.

Hermanns, R.L., M. Schleier, M. Böhme, L.H. Blikra, J. Gosse, S. Ivy-Ochs and P. Hilger 2017. Rock-avalanche activity in W and S Norway peaks after the retreat of the Scandinavian ice sheet. *Proc. Workshop on World Landslide Forum* 331–338.

Herring, T.A., T.I. Melbourne, M.H. Murray, M.A. Floyd, W.M. Szeliga, R.W. King, D.A. Phillips, C.M. Puskas, M. Santillan and L. Wang 2016. Plate Boundary Observatory and related networks: GPS data analysis methods and geodetic products. *Rev. Geophysics* 54, 759–808. https://doi.org/10.1002/2016RG000529

Hewitt, K., J.J. Clague and P. Deline 2011. Catastrophic rock slope failures and mountain glaciers. In: *Encyclopedia of snow, ice and glaciers.* Springer, Dordrecht, 112–126.

Hilger, P., R.L. Hermanns, J. Czekirda, K.S. Myhra, J.C. Gosse and B. Etzelmüller 2021. Permafrost as a first order control on long-term rock-slope deformation in (Sub-)Arctic Norway. *Quat. Sci. Rev.* 251, 106718. https://doi.org/10.1016/j.quascirev.2020.106718

Huggel, C., J.J. Clague and O. Korup 2012. Is climate change responsible for changing landslide activity in high mountains? *Earth Surface Processes and Landforms* 37, 77–91. https://doi.org/10.1002/esp.2223

Huggel, C., S. Zgraggen-Oswald, W. Haeberli, A. Kääb, A. Polkvoj, I. Galushkin and S.G. Evans 2005. The 2002 rock/ice avalanche at Kolka/Karmadon, Russian Caucasus: Assessment of extraordinary avalanche formation and mobility, and application of QuickBird satellite imagery. *Natural Hazards and Earth System Science* 5, 173–187. https://doi.org/10.5194/nhess-5-173-2005

Hugonnet, R., R. McNabb, E. Berthier, B. Menounos, S. Nuth *et al.* 2021. Accelerated global glacier mass loss in the early twenty-first century. *Nature* 592, 726–731. https://doi.org/10.1038/s41586-021-03436-z

Jónsdóttir, K., M. T. Gudmundsson, M. Pfeffer, A. Stefánsson, M. Parks *et al.* 2018. *Reawakening of Öræfajökull volcano monitored using a multidisciplinary approach.* EGU General Assembly Conference Abstracts, April, 17969.

Jónsson, Ó. B. 1974. *Berghlaup.* Prentverk Odds Björnssonar, Akureyri. In Icelandic, 9–96.

Kjartansson, G. 1967. Steinsholtshlaup, Central-South Iceland on January 15th, 1967. *Jökull* 17, 249–262. https://doi.org/10.33799/jokull1967.17.249

Kos, A., F. Amann, T. Strozzi, R. Delaloye, J. von Ruette and S. Springman 2016. Contemporary glacier retreat triggers a rapid landslide response, Great Aletsch Glacier, Switzerland. *Geophys. Res. Lett.* 43, 12,466-12,474. https://doi.org/10.1002/2016GL071708

Lacroix, P. and D. Amitrano 2013. Long-term dynamics of rockslides and damage propagation inferred from mechanical modeling. *J. Geophys. Res. Earth Surf.* 118, 2292–2307. https://doi.org/10.1002/2013JF002766

Lacroix, P., J. M. C. Belart, E. Berthier, Þ. Sæmundsson and K. Jónsdóttir 2022. Mechanisms of landslide destabilization induced by glacier-retreat on Tungnakvíslarjökull area, Iceland. *Geophys. Res. Lett.* 49(14). https://doi.org/10.1029/2022GL098302

Lee, R. E., J. C. Maclachlan and C. H. Eyles 2018. Landsystems of Morsárjökull, Skaftafellsjökull and Svínafellsjökull, outlet glaciers of the Vatnajökull Ice Cap, Iceland. *Boreas* 47, 1199–1217. https://doi.org/10.1111/bor.12333

Loughlin, S. C. 2002. Facies analysis of proximal subglacial and proglacial volcaniclastic successions at the Eyjafjallajökull central volcano, southern Iceland. *Geol. Soc. Spec. Publ.* 202, 149–178. https://doi.org/10.1144/GSL.SP.2002.202.01.08

Magnin, F., M. Krautblatter, P. Deline, L. Ravanel, E. Malet and A. Bevington 2015. Determination of warm, sensitive permafrost areas in near-vertical rockwalls and evaluation of distributed models by electrical resistivity tomography. *J. Geophys. Res.: Earth Surface* 120, 745–762. https://doi.org/10.1002/2014JF003351

Magnússon, E., F. Pálsson, H. Björnsson and S. Gudmundsson 2012. Removing the ice cap of Öraefajökull central volcano, SE-Iceland: Mapping and interpretation of bedrock topography, ice volumes, subglacial troughs and implications for hazards assessments. *Jökull* 62, 131–150. https://doi.org/10.33799/jokull2012.62.131

Matti, S. and H. Ögmundardóttir 2021. Local knowledge of emerging hazards: Instability above an Icelandic glacier. International *J. Disaster Risk Reduction* 58. https://doi.org/10.1016/j.ijdrr.2021.102187

McColl, S.T. 2012. Paraglacial rock-slope stability. *Geomorphology* 153–154, 1–16. https://doi.org/10.1016/j.geomorph.2012.02.015

McColl, S. T. and T. R. H. Davies 2012. Large ice-contact slope movements: Glacial buttressing, deformation and erosion. *Earth Surface Processes and Landforms* 38, 1102–1115. https://doi.org/10.1002/esp.3346

Mercier, D., E. Cossart , A. Decaulne, T. Feuillet, H. P. Jónsson and Þ. Sæmundsson 2013. The Höfðahólar rock avalanche (sturzström): Chronological constraint of paraglacial landsliding on an Icelandic hillslope. *Holocene* 23, 432–446. https://doi.org/10.1177/0959683612463104

Meredith, M. *et al.* 2019. Polar regions. In: Pörtner, H. O. *et al.* (eds.). *IPCC Special Report on the Ocean and Cryosphere in a Changing Climate*, 203–320. https://repository.library.noaa.gov/view/noaa/27411/-noaa_27411_DS1.pdf

Meyer, F. 2019. Spaceborne Synthetic Aperture Radar: Principles, Data Access, and Basic Processing Techniques. In: SAR Handbook: *Comprehensive Methodologies for Forest Monitoring and Biomass Estimation*, 17–24. https://doi.org/10.1016/b978-0-08-024732-8.50026-x

Morino, C., S. J. Conway, M. R. Balme, J. K. Helgason, Þ. Sæmundsson, C. Jordan, J. Hillier and T. Argles 2021. The impact of ground-ice thaw on landslide geomorphology and dynamics: two case studies in northern Iceland. *Landslides* 18, 2785–2812. https://doi.org/10.1007/s10346-021-01661-1

Morino, C., S. J. Conway, Þ. Sæmundsson. J. K. Helgason, J. Hillier, F. E. G. Butcher, .R. Balme, C. Jordan and T. Argles 2019. Molards as an indicator of permafrost degradation and landslide processes. *Earth Planet. Sci. Lett.* 516, 136–147. https://doi.org/10.1016/j.epsl.2019.03.040

Noël, B., G. Aðalgeirsdóttir, F. Pálsson, B. Wouters, S. Lhermitte, J. M. Haacker and M. R. van den Broeke 2022. North Atlantic Cooling is Slowing Down Mass Loss of Icelandic Glaciers. *Geophys. Res. Lett.* 49 https://doi.org/10.1029/2021GL095697

Norðdahl, H. and Ó. Ingólfsson 2015. Collapse of the Icelandic ice sheet controlled by sea-level rise? *arktos* 13. https://doi.org/10.1007/s41063-015-0020-x

Obu, J., S. Westermann, A. Bartsch, N. Berdnikov, H. H. Christiansen *et al.* 2019. Northern Hemisphere permafrost map based on TTOP modelling for 2000–2016 at 1 km^2 scale. *Earth Sci. Rev.* 193, 299–316. https://doi.org/10.1016/j.earscirev.2019.04.023

Pálsson, F., A. Gunnarsson, E. Magnússon, G. Aðalgeirsdóttir, S. Steinþórsson, K. Eiríksson and A. Björnsson 2022. *Vatnajökull: Mass balance, meltwater drainage and surface velocity of the glacial year 2021–2021.* Institute of Earth Sciences, U. Iceland and National Power Company of Iceland. Ann. Rep., 59 pp.

Penna, I., F. Magnin, P. Nicole, B. Etzelmüller, R. L. Hermanns, M. Böhme, L. Kristensen, F. Noël, M. Bredal and J. M. Dehls 2022. Permafrost controls the displacement rates of large unstable rock-slopes in subarctic environments. *Global and Planetary Change* 220, 104017. https://doi.org/10.1016/j.gloplacha.2022.104017

Peras, A., A. Decaulne, E. Cossart, J. Coquin and D. Mercier 2016. Répartition spatiale des glissements de terrain dans les fjords du nord-ouest d'Islande: Premiers resultants. *Geomorphologie: Relief, Processus, Environnement* 22, 25–35. https://doi.org/10.4000/geomorphologie.11303

Porter, P. R., M. J. Smart and T. D. L. Irvine-Fynn 2019. Glacial sediment stores and their reworking. In: *Geomorphology of Proglacial Systems* 157–176. https://doi.org/10.1007/978-3-319-94184-4_10

Reznichenko, N. V., T. R. H. Davies, J. Shulmeister and S. H. Larsen 2012. A new technique for identifying rock avalanche-sourced sediment in moraines and some paleoclimatic implications. *Geology* 40, 319–322. https://doi.org/10.1130/G32684.1

Roberts, M. J. and M. T. Gudmundsson 2015. Öræfajökull Volcano: Geology and historical floods. *Volcanogenic floods in Iceland: An assessment of hazards and risks at Öræfajökull and the Markarfljót outwash plain* 17–44. In: Pagneux, E., M. T. Gudmundsson, S. Karlsdóttir and M. J. Roberts (eds.). *Volcanogenic floods in Iceland: An assessment of hazards and risks at Öræfajökull and the Markarfljót outwash plain.* 17–44. IMO, IES-UI, NCIP-DCPEM, Reykjavík.

Rosen, P. A., E. Gurrola G. F. Sacco and H. Zebker 2012. The InSAR Scientific Computing Environment. In: *EUSAR 2012; 9th European conference on synthetic aperture radar*, 730–733. VDE.

Sæmundsson, K. 1978. Fissure swarms and central volcanoes of the neovolcanic zones of Iceland. In: *Crustal evolution in northern Britain and adjacent regions. Geological J. Liverpool* 10, 415–432.

Sæmundsson, Þ., J. K. Helgason, D. Ben-Yehoshua and B. H. Bergsson 2019. Risk of major rock slope failure at the Svínafellsheiði mountain, SE Iceland. Geoph. Res. Abstracts, EGU 21, 9650.

Sæmundsson, Þ., C. Morino, J. K. Helgason, S. J. Conway and H. G. Pétursson 2018. The triggering factors of the Móafellshyrna debris slide in northern Iceland: Intense precipitation, earthquake activity and thawing of mountain permafrost. *Science of the Total Environment* 621, 1163–1175. https://doi.org/10.1016/j.scitotenv.2017.10.111

Sæmundsson, Þ., I. A. Sigurðsson, H. G. Pétursson, H. P. Jónsson, A. Decaulne and M. J. Roberts 2011. The rock avalanche which fell on the Morsárjökull outlet glacier, 20th of March 2007. *Náttúrufræðingurinn* 81 (3–4), 132–141.

Schleier, M., R. L. Hermanns, J. Rohn and J. C. Gosse 2015. Diagnostic characteristics and paleodynamics of supraglacial rock avalanches, Innerdalen, Western Norway. *Geomorphology* 245, 23–39. https://doi.org/10.1016/j.geomorph.2015.04.033

Schmidt, L. S., G. Aðalgeirsdóttir, F. Pálsson, P. L. Langen, S. Guðmundsson and H. Björnsson 2019. Dynamic simulations of Vatnajökull ice cap from 1980 to 2300. *J. Glaciology* 66, 97–112. https://doi.org/10.1017/jog.2019.90

Schöpa, A., W. A. Chao, B. P. Lipovsky, N. Hovius, R. S. White, R. G. Green and J. M. Turowski 2018. Dynamics of the Askja caldera July 2014 landslide, Iceland, from seismic signal analysis: Precursor, motion and aftermath. *Earth Surface Dynamics* 6, 467–485. https://doi.org/10.5194/esurf-6-467-2018

Sharma, K., S. Self, S. Blake, T. Thordarson and G. Larsen 2008. The AD 1362 Öræfajökull eruption, S.E. Iceland: Physical volcanology and volatile release. *J. Volc. Geoth. Res.* 178, 719–739. https://doi.org/10.1016/j.jvolgeores.2008.08.003

Shugar, D. H. *et al.* 2021. A massive rock and ice avalanche caused the 2021 disaster at Chamoli, Indian Himalaya. *Science* 373, 300–306. https://doi.org/10.1126/science.abh4455

Sigmundsson, F. 2021. Icelandic Volcanoes Supersite 2020–2021, 1–22. http://geo-gsnl.org/wp-content/-Documents/Supersites/Iceland/Reports/Icelandic_-Volcanoes_Biennial_Report_2018_2019r.pdf

Sigurdsson, O. and R. S. Williams 1991. Rockslides on the terminus of Jökulsárgilsjökull, southern Iceland. *Geografiska Annaler*, Series A 73 A, 129–140. https://doi.org/10.1080/04353676.1991.11880338

Soldati, M. 2013. Deep-seated Gravitational Slope Deformation. In: *Encyclopedia of Earth Sciences Series*. Springer, Netherlands, 151–155.

Soldati, M. A. Corsini and A. Pasuto 2004. Landslides and climate change in the Italian Dolomites since the Lateglacial. *Catena* 55, 141–161. https://doi.org/10.1016/S0341-8162(03)00113-9

Spreafico, M. C., P. Sternai, F. Agliardi 2021. Paraglacial rock-slope deformations: sudden or delayed response? Insights from an integrated numerical modelling approach. *Landslides* 18, 1311–1326. https://doi.org/10.1007/s10346-020-01560-x

Stead, D. and E. Eberhardt 2013. Understanding the mechanics of large landslides. *Italian J. Engineering Geology and Environment.* Special issue: The 1963 Vajont Landslide (Northeast Alps, Italy), 85–112. https://doi.org/10.4408/IJEGE.2013-06.B-07

Stoffel, M. and C. Huggel 2012. Effects of climate change on mass movements in mountain environments. *Progr. Phys. Geography* 36, 421–439. https://doi.org/10.1177/0309133312441010

Storni, E., M. Hugentobler, A. Manconi and S. Loew 2020. Monitoring and analysis of active rockslide-glacier interactions (Moosfluh, Switzerland). *Geomorphology* 371, 107414. https://doi.org/10.1016/j.geomorph.2020.107414

Svennevig, K., T. Dahl-Jensen, M. Keiding, J. Peter Merryman Boncori, T. B. Larsen, S. Salehi, A. Munck Solgaard and P. H. Voss 2020. Evolution of events before and after the 17 June 2017 rock avalanche at Karrat Fjord, West Greenland - A multidisciplinary approach to detecting and locating unstable rock slopes in a remote Arctic area. *Earth Surface Dynamics* 8, 1021–1038. https://doi.org/10.5194/esurf-8-1021-2020

Svennevig, K., M. Keiding, N. J. Korsgaard, A. Lucas, M. Owen, M. D. Poulsen, J. Priebe, E. V. Sørensen and C. Morino 2022. Uncovering a 70-year-old permafrost degradation induced disaster in the Arctic, the 1952 Niiortuut landslide-tsunami in central West Greenland. *Science of The Total Environment* 160110. https://doi.org/10.1016/j.scitotenv.2022.160110

Tharp, T. M. 2003. Cover-collapse sinkhole formation and soil plasticity. *Sinkholes and the engineering and environmental impacts of karst* 110–123. https://doi.org/10.1061/40698(2003)9

Thompson, A. 1988. Historical development of the proglacial landforms of Svínafellsjökull and Skaftafellsjökull, southeast Iceland. *Jökull* 38, 17–30. https://doi.org/10.33799/jokull1988.38.017

Thorarinsson, S. 1958. The Öræfajökull Eruption of 1362. *Acta Naturalia Islandica* 2, 100.

Thordarson, T. and G. Larsen 2007. Volcanism in Iceland in historical time: Volcano types, eruption styles and eruptive history. *J. Geodynamics* 43, 118–152. https://doi.org/10.1016/j.jog.2006.09.005

Torfason, H. and H. B. Jónsson 2005. Jarðfræði við norðvestanverðan Mýrdalsjökul. *Hættumat vegna eldgosa og hlaupa úr vestanverðum Mýrdalsjökli og Eyjafjallajökli* 45–74. Ríkislögreglustjórinn, Háskólaútgáfan, Reykjavík.

Walker, C. 1991. North Atlantic ocean crust and Iceland. In: Floyd, P. A. (ed.). *Oceanic Basalts*, 311–352, Springer, Boston, MA.

Weingaertner, M. 2007. Iceland-095. https://www.flickr.com/photos/marcoweingaertner/-968525742/in/photostream/ (07.09.2023)

Wyllie, D. C. 2017. *Rock slope engineering: Civil applications*, fifth edition, 27–58, CRC Press.

Zemp, M., M. Huss, E. Thiebert, N. Eckert, R. McNabb *et al.* 2019. Global glacier mass changes and their contributions to sea-level rise from 1961 to 2016. *Nature* 568, 382–386. https://doi.org/10.1038/s41586-019-1071-0

Þórarinsson, S. 1956. On the variations of Svínafellsjökull, Skaftafellsjökull and Kvíárjökull in Öræfi. *Jökull* 6, 1–15. https://doi.org/10.33799/jokull1956.06.001

Table S1. Overview of the raster data used in this study. – *Yfirlit yfir rastargögnin sem notuð voru í þessari rannsókn.*

Data type	method	Year	Source	Pixel size [m]
Aerial imagery	single frame	1968	LMÍ	∼0.5
Aerial imagery	single frame	1980	LMÍ	∼0.5
Aerial imagery	photogrammetry	1994	LMÍ	∼0.3
Aerial imagery	photogrammetry	2003	Loftmyndir ehf.	0.1
Satellite imagery	photogrammetry	2009	QuickBird 2 (Maxar)	0.5
Satellite imagery	photogrammetry	2012	WorldView 2 (Maxar)	0.41
Aerial imagery	photogrammetry	2013	Loftmyndir ehf.	0.1
UAV imagery	photogrammetry	2016	(Ben-Yehoshua, 2016)	0.18
Aerial imagery	photogrammetry	2017	Loftmyndir ehf.	0.1
UAV imagery	photogrammetry	2017	this study	0.014
UAV imagery	photogrammetry	2018	(Ben-Yehoshua and Gunnarson, 2018)	0.034
UAV imagery	photogrammetry	2020	this study	0.05
Aerial imagery	photogrammetry	2021	Loftmyndir ehf.	0.1
DEM	Moraine extents	1890	Hannesdóttir *et al.* (2015)	50
DEM	photogrammetry	1945	Belart *et al.* (2020)	5
DEM	photogrammetry	1960	Belart *et al.* (2020)	5
DEM	photogrammetry	1982	Belart *et al.* (2020)	5
DEM	photogrammetry	1994	Belart *et al.* (2020)	5
DEM	photogrammetry	2003	Loftmyndir ehf.	10
DEM	GPS profile interpolation	2005	Magnússon *et al.* (2012)	10
DEM	Lidar	2011	Jóhannesson *et al.* (2013)	2
DEM	photogrammetry	2013	ÍslandsDEMv1, LMÍ	2
DEM	photogrammetry	2017	Belart *et al.* (2020)	3.1
DEM	photogrammetry	2019	Sigmundsson (2021)	4
DEM	photogrammetry	2020	this study	0.05
DEM	photogrammetry	2021	Sigmundsson (2021)	2
DEM (subglacial)	RES	2005/2006	Magnússon *et al.* (2012)	20

Table S2. Summary of produced interferograms. – *Samantekt framleiddra bylgjuvíxlamynda.*

Sentinel -1 track	Flight direction	Heading [°]	Incline angle [°]	Number of interferograms
118	Ascending	350.7	39.4	112
147	Ascending	347.0	44.8	132
111	Descending	191.2	33.1	111
9	Descending	193.0	33.1	115